Computer Modeling in Engineering & Sciences

Tech Science Press

https://doi.org/10.32604/cmes.2026.087442

ARTICLE

Effect of Strut Modelling on Predicted Strain and Damage Initiation in a Full-Scale Composite Helical Crossflow Tidal Turbine Foil

Tenis Ranjan Munaweera Thanthirige[1,*], Michael Flanagan[1], Ciaran Kennedy[1], Yadong Jiang[2], Tomas Flanagan[3], Micheal O'Conghaile[3], Jeffwin George[4], Michael Walls[4], Clement Courade[5], Conor Dillon[5], Patrick Cronin[5], Edward M. Fagan[6], Jamie Goggins[1] and William Finnegan[1,*]

[1]Construct Innovate and Ryan Institute, School of Engineering, University of Galway, Galway, Ireland
[2]Civil Engineering, Atlantic Technical University, Galway, Ireland
[3]ÉireComposites Teo, An Choill Rua, Inverin, Co., Galway, Ireland
[4]Composites Testing Laboratory Tástáil Teo, Údarás Industrial Estate An Choill Rua, An Choill Rua, Inverin, Galway, Ireland
[5]ORPC Ireland, Dublin, Ireland
[6]Zero Nexus Inc., Midland, ON, Canada

*Corresponding Authors: Tenis Ranjan Munaweera Thanthirige. Email: tenisranjanmt@universityofgalway.ie; William Finnegan. Email: william.finnegan@universityofgalway.ie

Received: 16 June 2026; Accepted: 11 September 2026; Published: 21 October 2026

ABSTRACT: This study presents the experimental correlation and partial validation of a finite element (FE) model of a 5 m long helical crossflow tidal turbine foil that forms part of a two-turbine 80 kW marine hydrokinetic system. Full-scale structural test data were obtained from a programme conducted according to the industry standards DNV-ST-0164 and IEC TS 62600-3:2020, using modern measuring tools. Under the representative 30% idealised static load case FE predicted and measured spanwise strain distributions follow the same trend, with deviations within about 10% away from the supports but reaching 28% for fibre-optic sensors and 45% for strain-gauge channels at the cantilever fixed end. Modal correlation is partial because two LSV-identified frequencies match the FE modes within 1.5% while the measured 37.50 Hz mode has no FE counterpart and the predicted 52.59 Hz mode was not observed in the scanned region. Predicted Hashin damage initiation zones are spatially consistent with the damage recorded at the final test stage, though initiation load was not verified and damage progression was outside the scope of this work. Propagating coupon properties measured after six months of immersion at 50°C gave an approximately 2% increase in FE model predicted strain, reported as a preliminary indication rather than a quantified degradation rate. The work establishes an experimentally correlated FE framework for helical crossflow foils and identifies what is required to convert that correlation into full validation.

KEYWORDS: Finite element analysis; structural testing; composite materials; composite structures; tidal energy; marine renewable energy; model validation; accelerated ageing

1 Introduction

Tidal energy converters (TECs) are emerging as a viable renewable technology for harnessing the highly predictable energy potential of tidal currents to generate sustainable electricity. Among marine renewables, tidal stream energy is particularly attractive due to its reliability and its potential to contribute to a balanced and resilient energy mix [1,2]. However, for TECs to compete effectively with other renewable technologies, it is essential to reduce their levelised cost of energy (LCOE) while ensuring robust performance

Copyright © 2026 The Authors. Published by Tech Science Press. This work is licensed under a Creative Commons Attribution 4.0 International License, which permits unrestricted use, distribution, and reproduction in any medium, provided the original work is properly cited.

and long-term reliability in harsh marine environments. A critical challenge in this context lies in the structural integrity of turbine blades/foils, which are key load-bearing components subjected to cyclic hydrodynamic loading, debris impact, erosion, and biofouling. These conditions make blades/foils especially susceptible to damage and failure that directly affect system efficiency, maintenance demands, and overall lifecycle costs [1,3]. To mitigate such risks, comprehensive structural testing programmes are typically required for new tidal turbine designs prior to commercial deployment. These programmes comply with DNV-ST-0164 and IEC TS 62600-3:2020, established industry standards involving substantial time and investment [4,5]. In parallel, advancements in materials, manufacturing techniques, and design methodologies, particularly the implementation of advanced fibre-reinforced composites, are enabling the development of lighter, stronger, and more durable turbine blades/foils. However, the increasing complexity associated with these innovations further amplifies the need for efficient and scalable evaluation methods beyond purely experimental approaches.

Within this framework, the development of reliable finite element (FE) models that are validated against experimental data has become a critical research direction [6]. Such models enable cost-effective assessment of structural performance, facilitate iterative design optimisation and support the evaluation of manufacturing variations without the need for repeated full-scale testing. Furthermore, validated FE models provide a strong foundation for the integration of digital twin technologies and machine learning techniques by offering enhanced predictive capabilities and enabling data-driven decision-making for future design improvements not only for tidal turbine systems but also for wind turbines [7]. Accurate acquisition and processing of experimental data are essential to this approach. Recent advancements in sensing and measurement technologies have significantly improved the precision and efficiency of structural testing, allowing for more reliable capture of blade/foil performance under realistic loading conditions [8]. At the same time, incorporating dynamic analysis during both design and testing phases is crucial to ensure that the natural frequencies and mode shapes of the system do not coincide with operational excitation sources, thereby reducing the risk of resonance-induced failures. Properly validated FE models can effectively replicate these dynamic characteristics and align closely with experimental observations.

Full-scale experimental validation of composite blade and foil FE models has developed steadily over the past decade, but the published body of work remains concentrated on axial-flow turbine systems. University of Galway reported FE modelling, manufacture and structural testing of a full-scale 1 MW axial tidal turbine blade by establishing a workflow in which shell-based laminate models are correlated against strain gauge measurements from static proof loading [6]. Later, the research work was extended to study the seawater degradation of a fibre-reinforced blade considering the same tidal turbine blade system [9]. University of Edinburgh examined parasitic effects introduced at load introduction points during full-scale composite tidal blade tests and showed that local strain fields near loading pads are systematically disturbed relative to idealised predictions [10]. Comparable lessons have been drawn from the offshore wind sector, where lifetime extension of support structures and the treatment of stress concentration factors in tubular joints have both been reviewed in detail [11,12]. What these studies share is a straight, prismatic or mildly twisted load path. A helical crossflow foil does not offer that. Its chord rotates continuously along the span; it is supported at three discrete strut positions rather than at a single root flange, and the load must be introduced perpendicular to a chord whose orientation changes at every station. The consequence is that neither the boundary condition idealisations nor the sensor placement strategies developed for axial blades transfer directly.

Within this background, several important gaps remain to be addressed to advance the structural design, validation and lifetime assessment of tidal energy technologies. Physical testing remains essential, but testing alone cannot provide a complete understanding of structural behaviour across the full geometry, operating envelope and range of material conditions relevant to tidal applications. Full-scale testing typically

provides measurements at a limited number of discrete locations and under a defined set of experimentally achievable load cases. Consequently, important regions of the structure may remain insufficiently characterised, particularly where instrumentation is constrained by accessibility, durability, cost or the practical limitations of long-duration fatigue testing. A key gap is therefore the development and experimental validation of FE models capable of extending the information obtained from full-scale testing to the wider structural field. A validated model can provide insight into regions between measurement locations, identify critical structural responses that may not be directly measurable, and enable the effects of alternative loading conditions to be assessed without requiring a new physical test for every configuration [8]. Such capability is particularly important for evaluating material substitutions, structural modifications, manufacturing variations and changes in material properties associated with ageing and environmental exposure [9,13]. This need is especially noticeable for complex tidal turbine geometries in which the structural response cannot be adequately inferred from conventional section properties or simplified beam representations. Helical crossflow foils, for example, experience continuously varying geometric orientation along the span while structural loads are transferred through multiple discrete support locations [2]. These characteristics can produce complex and spatially varying strain, deformation, vibration, and damage patterns. A better understanding of how these responses develop across the complete structure is therefore required to support reliable structural design and assessment.

Another significant gap concerns the influence of the marine environment on structural performance over extended operating periods. Seawater exposure can alter material properties and consequently, stiffness, load distribution, dynamic characteristics and local stress and strain concentrations. However, the extent to which environmentally induced changes in material properties influence the structural response of complex tidal turbine components remains insufficiently understood. There is a particular need to establish how property degradation propagates through the structure and how this may affect fatigue performance, modal behaviour, damage accumulation and ultimately structural reliability.

Addressing these gaps requires closer integration of full-scale experimental testing with experimentally validated FE modelling. Such an approach can provide a framework for linking measured structural behaviour with the underlying response of the complete component while enabling systematic investigation of conditions that cannot feasibly be reproduced through physical testing alone. The resulting capability would support more robust design methods, improved prediction of structural lifetime, more effective assessment of environmental degradation and more informed decisions regarding material selection, maintenance and end-of-life management. Collectively, these gaps highlight the need for experimentally validated modelling approaches that can capture the structural behaviour of full-scale tidal turbine components under realistic loading and environmental conditions. Progress in this area is important for reducing uncertainty in structural design, improving confidence in long-term performance predictions and supporting the development of more reliable and cost-effective tidal energy technologies.

2 Methodology

The primary aim of this study is to develop and experimentally correlate an FE model of a 5 m long crossflow helical shape tidal turbine foil using full-scale structural test data and to apply the correlated model to identify opportunities for improving structural reliability and performance. To support that aim, this paper presents the following objectives:

I. To develop an FE model of a 5 m long crossflow helical shape tidal turbine foil to a level that supports independent assessment, including a mesh sensitivity study, the boundary condition treatment at the three strut positions and the representation of the hybrid bolted and bonded joints.

II. To correlate the FE-predicted spanwise strain distribution against the fibre Bragg grating (FBG) and strain gauge measurements recorded under the 30% idealised static load case, applied in accordance with DNV-ST-0164 and IEC TS 62600-3:2020, and to quantify the level of agreement by region.
III. To correlate the FE-predicted natural frequencies and mode shapes with those identified using a laser scanning vibrometer (LSV) and to determine which modes are matched and which remain unmatched, along with the likely reasons for the discrepancies.
IV. To establish whether the damage initiation regions predicted using Hashin's criteria correspond spatially to the damage observed on the article during the structural testing programme.
V. To investigate the structural performance of advanced carbon fibre prepreg composites by incorporating both conditioned (accelerated ageing to simulate water absorption effects) and unconditioned coupon-scale test data into the FE model and to demonstrate the value of a correlated FE framework for enabling future design and performance enhancements.
VI. To state explicitly which parts of the resulting correlation reach the standard of validation, and which do not, so that the model is applied within the bounds the evidence supports.

To achieve the objectives, a structured three-phase methodology is employed as shown in Fig. 1, integrating experimental testing with advanced FE modelling to ensure both accuracy and applicability of the results. In Phase 1, static testing of a tidal turbine foil is performed under representative idealised loading conditions as part of a full-scale structural test programme. The testing is conducted in compliance with DNV-ST-0164 and IEC TS 62600-3:2020 standards by ensuring the generation of high-quality experimental data that accurately captures the foil's structural response under realistic loading scenarios. This phase focuses on capturing global and local structural responses by including deflection, strain distribution and failure modes, thereby establishing a reliable benchmark dataset. Phase 2 involves the development of a detailed FE model of the foil by incorporating accurate geometric representation, boundary conditions and material properties. The model is calibrated and validated against the full-scale test data through iterative refinement to ensure that FE predictions closely match experimental observations. In Phase 3, material-level investigations are integrated into the modelling framework by incorporating data from coupon-scale testing of two advanced carbon fibre prepreg composites, including both unconditioned specimens and those subjected to accelerated ageing to mimic water absorption and environmental degradation. This enables the FE model to account for material variability and degradation effects, thereby improving its predictive capability under realistic operating conditions. This phase also highlights the broader significance of employing a validated FE approach in reducing reliance on costly experimental campaigns while enabling efficient, data-driven enhancements to tidal turbine foil design and performance.

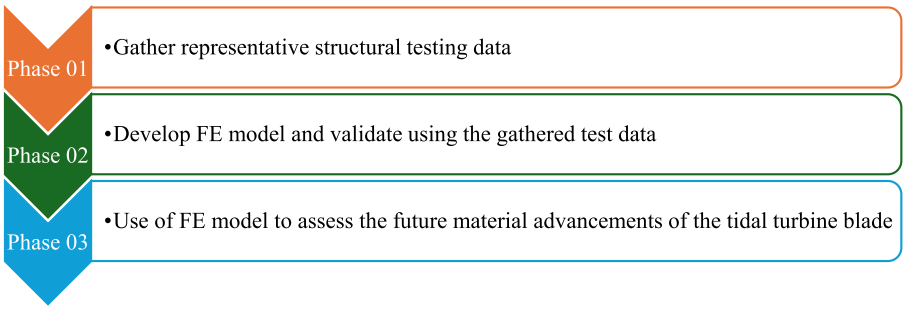


Figure 1: Methodology of the study.

2.1 Tidal Turbine Model

For this study, a helical-shaped foil from an 80 kW dual-rotor crossflow tidal turbine system was selected. Each rotor was equipped with three helical-shaped foils, and the 5 m long foils were manufactured from carbon-fibre prepreg composite materials. Fig. 2 shows a computer-generated model of the tidal turbine system, comprising the main shaft and the three fibreglass struts that connect the three turbine foils together. For conducting structural testing, one 5 m long tidal turbine foil was manufactured and was secured to the reinforced concrete reaction floor in the Large Structures Testing Laboratory at the University of Galway, as shown in the computer-generated model in Fig. 3. This helical-shaped tidal turbine foil was manufactured using a combination of unidirectional (UD), biaxial (BIAX), and WOVEN carbon fibre prepreg composites, each with an areal weight of 300 g/m^2 supplied by SHD Composites. One tidal turbine foil consists of approximately 80% UD fibres and has a mass of 26.75 kg at full scale. In this setup, the foil was attached to a central shaft using three glass fibre struts, each manufactured from a fiberglass powder epoxy composite with an areal weight of 1200 g/m^2. Each strut had a mass of 14.5 kg. The material properties of the materials used for manufacturing the tidal turbine foil are mentioned in Table 1. This material selection enabled high manufacturing quality while achieving a lightweight yet robust structural design. Compared to dry carbon fibre fabrics, carbon fibre prepreg composites provide greater consistency and improved mechanical performance, as the fibres are pre-impregnated with a precise amount of resin, reducing variability while improving fibre-to-resin ratio control and simplifying the manufacturing process for enhancing the quality and repeatability of the final composite structure.

2.2 Instrumentation Schedule

In accordance with the study methodology, data obtained under a representative idealised loading condition were used to validate the FE model. A summary of the instrumentation employed in this study is provided in Table 2. For the purpose of comparing the FE model predictions with experimentally measured dynamic properties, an LSV was utilised as an advanced, non-contact measurement system. This technique enabled accurate capture of the structural vibration response, facilitating a reliable assessment of the FE model performance. To ensure accurate measurement of strain distribution along the spanwise direction, both strain gauges and FBG sensors were employed. The use of these advanced sensing techniques enabled strong validation of the FE model by providing two independent datasets for strain distribution. Fig. 4 shows a few locations of the installed strain gauges and the FBG sensors, and the exact locations of the strain gauges and FBG sensors on the top surface were previously published in *Engineering Structures* in 2025 [2].

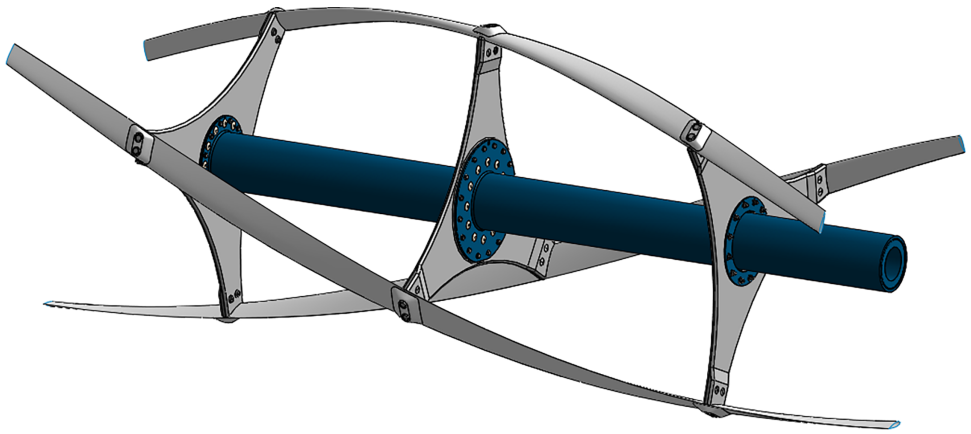


Figure 2: Computer-generated model of a single rotor from an 80 kW tidal turbine system.

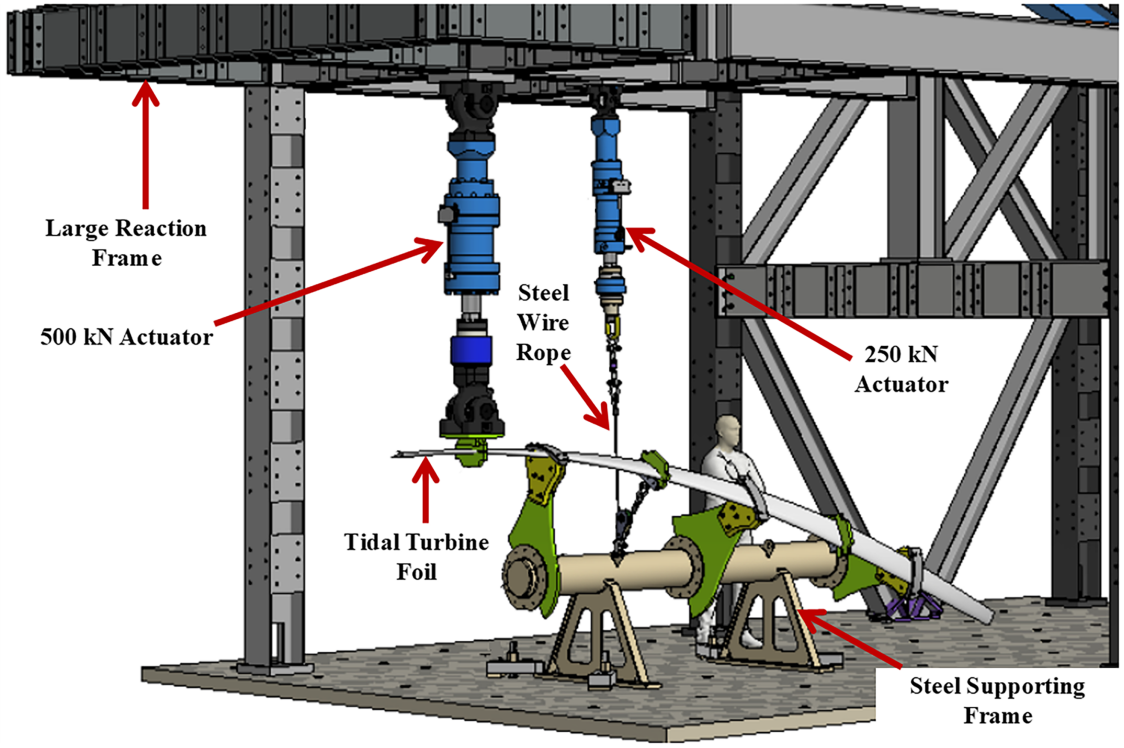


Figure 3: Computer generated structural testing arrangement.

Table 1: Baseline laminate material properties.

Prepreg Material	Cure Ply Thickness (mm)	Number of Plies	Orthotropic Material Properties			
			E_1 (MPa)	E_2 (MPa)	G_{12} (MPa)	Poisson's Ratio
WOVEN	0.223	1	55,700	55,100	3000	0.05
BIAX	0.231	6	54,000	54,000	4000	0.04
UD	0.306	27	110,450	7770	3600	0.30

Table 2: Instrumentation used in the study.

Measurement	Quantity	Location	Sensor Type
Strain	11	Foil, Strut	Linear Strain Gauge (strain in single direction)
	7	Foil	Rosette Strain Gauge (strain in multiple direction)
	2	Foil	FBG
Displacement	1	Foil tip	String pot
	1	Foil tip	Laser displacement sensor
Load	2	Servo hydraulic Actuators	In-built load cell
Surface velocity	1	Foil	LSV system (out-of-plane velocity, integrated to displacement)

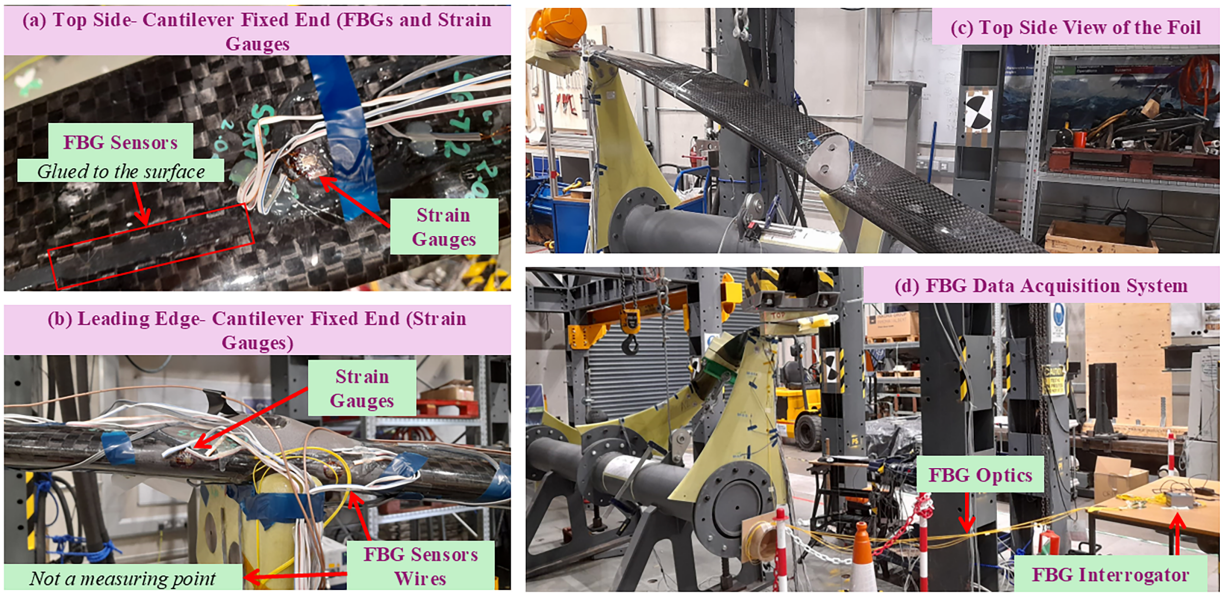


Figure 4: Installed strain gauges and FBG sensors on the foil surface.

2.3 LSV System Setup

The study aims to assess the dynamic response obtained from the LSV system against the results predicted by the FE model with the objective of further validating the model. The LSV system provides high-resolution, non-contact vibration measurements and is capable of accurately capturing natural frequencies as well as detailed mode shape characteristics. These capabilities offer significant advantages over conventional accelerometer-based methods, particularly in terms of spatial resolution and measurement reliability. Here, for monitoring the flapwise dynamic the LSV system was set up as shown in Fig. 5 and the laser scanning head was strategically positioned below the cantilever section of the tidal turbine foil to accurately measure the bottom surface of the turbine foil by ensuring it was perpendicular to the surface for optimal data collection. Moreover, to undertake comprehensive analysis, 21 scanning points were selected within a rectangular scanning area highlighted in the Fig. 5. Excitation was applied with an instrumented impact hammer at the cantilever tip, at a marked location held constant across all dynamic tests, with the hammer pre-triggered by 10% so that the full excitation was captured. The measured response quantity is out-of-plane surface velocity from which displacement mode shapes are obtained by integration. Natural frequencies were extracted by applying a Fast Fourier Transform to the recorded time-domain signal, and modes were identified by peak picking from the resulting magnitude spectra and confirmed against the animated mode shapes generated by the LSV software. The scanning range was set from 0 to 80 Hz for the tests reported here by following an initial survey over 0 to 200 Hz, which confirmed that no further modes of the foil were observable above 80 Hz. Repeatability of the dynamic response was checked before the testing programme began and was found to be within 0.75 Hz [8]. Modal damping was not extracted, since the dynamic testing in this campaign was directed at tracking frequency shifts as an indicator of damage rather than at full modal identification.

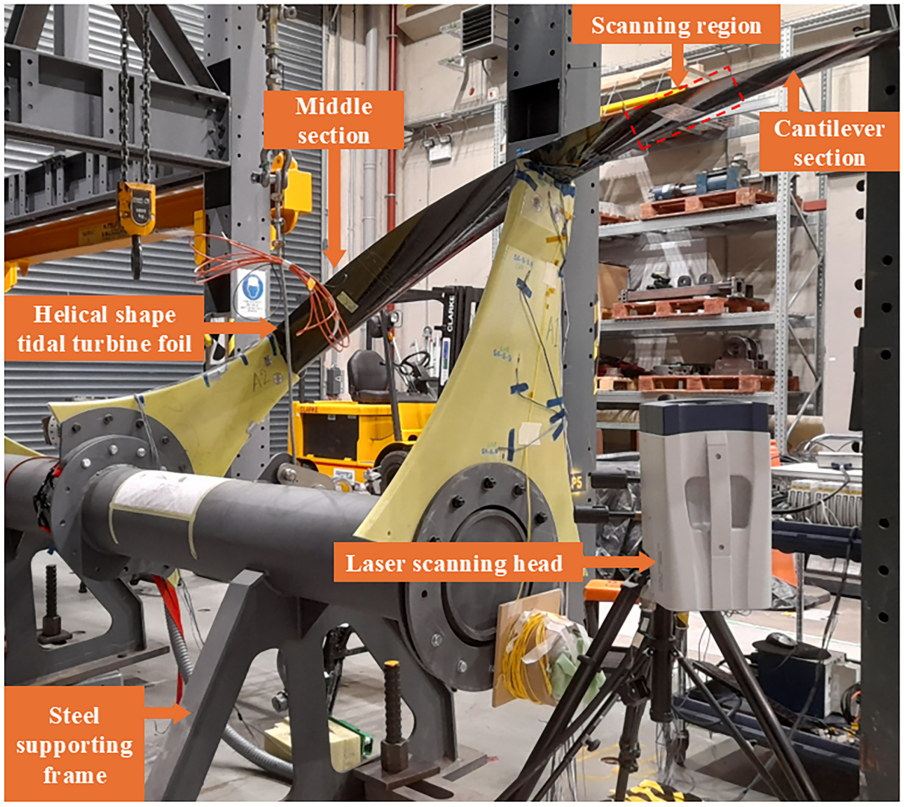


Figure 5: LSV setup.

2.4 Representative Static Testing Setup

The static case reported here corresponds to 30% of the idealised design load, which was applied during the initial stage of the static testing programme. The idealised design load is the extreme quasi-static hydrodynamic load case derived by ORPC Ireland for the 80 kW rotor and resolved into two equivalent point loads, one at the cantilever tip station and one at the higher middle section. During initial static testing, the load scale factor was stepped from 10% to 30% by giving cantilever tip forces between 2640 and 7890 N and mid-section forces between 2520 and 7360 N [2]. The 30% level is treated here as a representative case study rather than as a complete load envelope according to the DNV-ST-0164 and IEC TS 62600-3:2020 standards. Two servo hydraulic actuators were utilised for the static testing, with a capacity of 500 kN actuator positioned at the cantilever end of the foil and a 250 kN actuator employed for the higher middle section, as illustrated in Fig. 6. The 500 and 250 kN figures are the rated capacities of the two servo hydraulic actuators installed in the laboratory testing frame, not the applied loads. Both actuators were operated well below capacity for this structural testing programme. Moreover, the middle segment of the foil was subjected to loading using a steel rope and a pulley system, as shown in Fig. 6, with the loading directions highlighted by red arrows. Considering the helical geometry of the foil, the composite loading pads and the loading mechanism were designed to apply the load to the mid-span section at an angle of 40° from the vertical, thereby ensuring that the loading direction was perpendicular to the chord of the foil. The detailed setup of the static testing program is shown in Fig. 7, highlighting the loading directions and the approximated bending moment patterns resulting from actuator loading to provide a better understanding of the testing configuration.

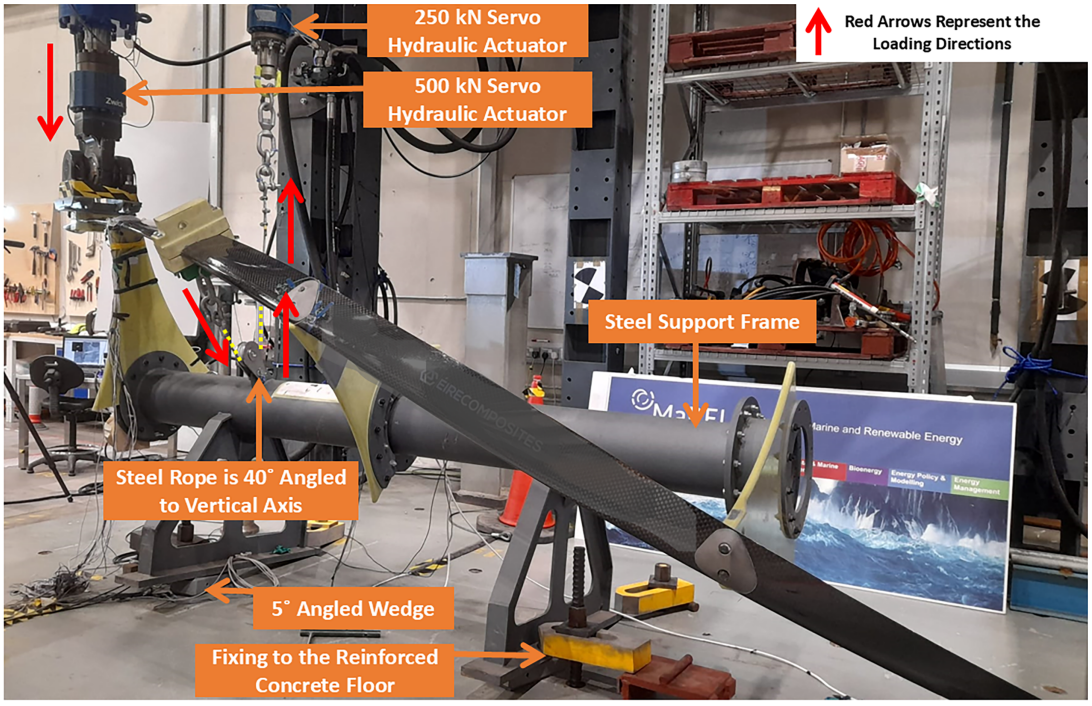


Figure 6: Static test configuration at University of Galway [2].

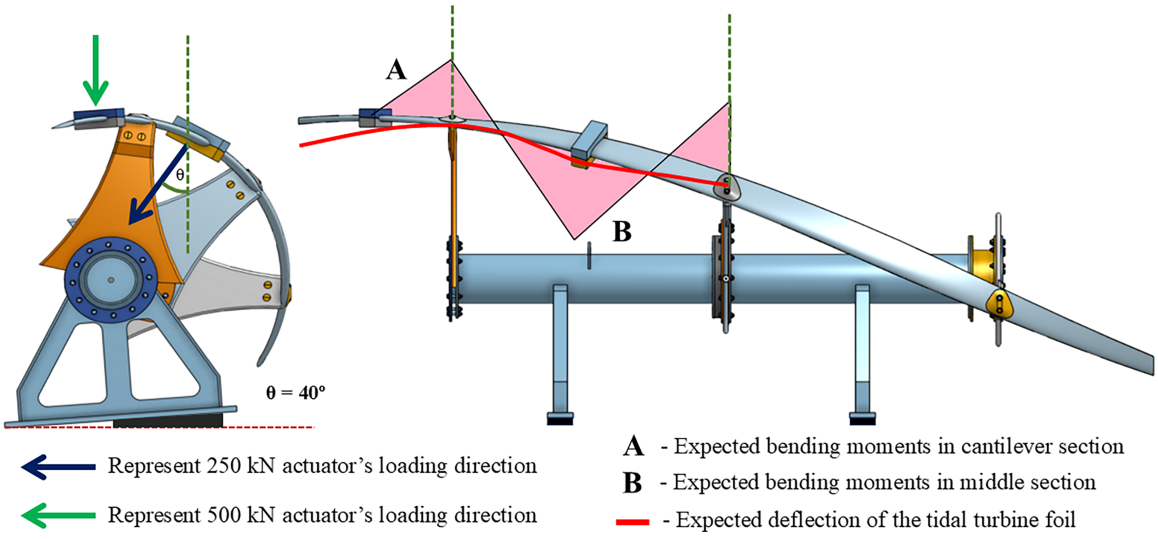


Figure 7: Schematic diagram for static test configuration.

Here, the 250 kN actuator applied load downwards using a wire rope and a pulley, although its original displacement was in the upward direction, while the 500 kN actuator applied downwards loads on the cantilever tip end of the foil. In here, the load applied by the two actuators was measured using installed load cells, while the hydraulic actuators' loading process was controlled by CUBUS software [14]. Moreover, drawing upon experience and knowledge gained from structural testing aligned with these two standards, it was determined that loading the foil to the 6-h duration specified in IEC TS 62600-3:2020 was

unnecessary [15]. Therefore, the hydraulic system followed a programmed sequence: a 30-s ramp-up, a 40-s dwell, and a 30-s ramp-down, all managed through a custom-coded load control program. In addition, three ramp cycles were executed for each test to ensure repeatability and data recording accuracy.

2.5 FE Model Development

Abaqus 2023 software version was used to conduct the FE simulations for the assembly of the foil struts [16]. The FE model generated from the Abaqus 2023 software is illustrated in Fig. 8. With reference to the model, the material major directions for each ply were carefully defined to align with the helical shape of the foil by ensuring alignment with the specific design principles of the composite laminate structure specified by ORPC Ireland. Additionally, the stacking sequence and orientations of the three carbon fibre prepreg fabrics were defined in accordance with the overall laminate design.

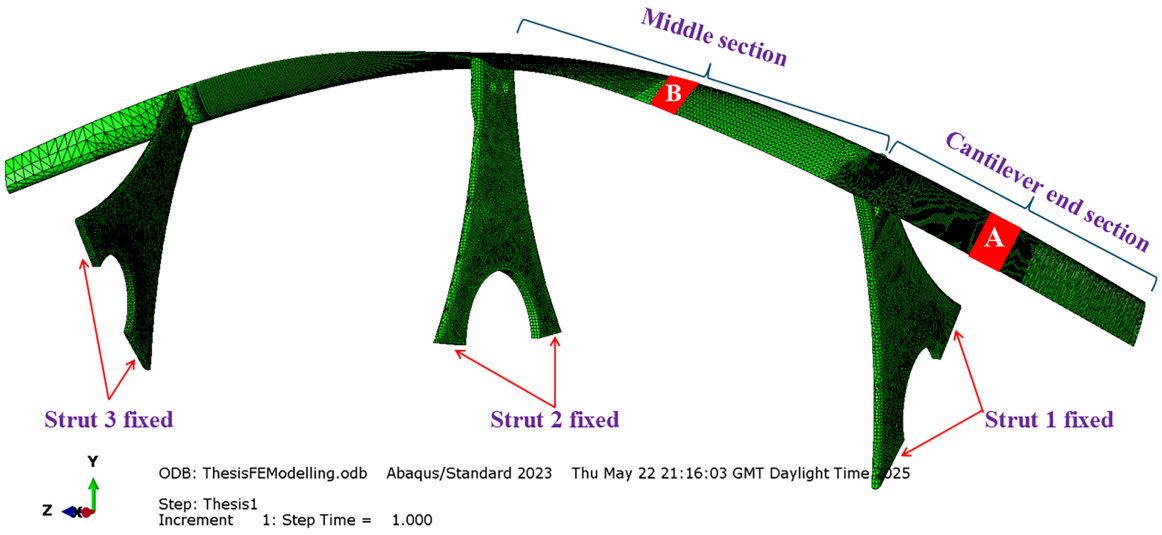


Figure 8: FE mesh model generated for tidal turbine foil and the struts.

The boundary conditions of the FE model were established by restricting all active structural degrees of freedom at the base of each of the three struts, where they connect to the central shaft, as shown in Fig. 8. The struts themselves are represented as discrete structural bodies, so that the load transferred from the foil is carried through the strut geometry before reaching the restrained boundary. This differs from the initial FE model reported for this foil, in which the struts were not modelled, and the restraint was applied directly at the three strut attachment positions on the foil [2]. That treatment placed a rigid boundary at the points of highest strain gradient and removed the compliance of the support structure from the analysis. Resolving the struts explicitly restores that compliance and relocates the restrained boundary away from the region of interest. The consequence for the predicted strain field is confined to the cantilever fixed end, where it is substantial and is quantified with the strain comparison presented later in this paper.

The FE mesh of the assembly was constructed using both 3-node triangular (S3) and 4-node quadrilateral reduced-integration (S4R) general-purpose shell elements throughout. Quadrilateral elements were used wherever the surface admits a regular mesh, while triangular elements were retained in the transition regions forced by the helical geometry where they conform to the continuously twisting surface without distortion. The foil is meshed with 22,931 nodes and 39,186 elements at the 5 mm global element size employed for all analyses reported in this paper. The three struts were meshed separately using the same element formulations, with 25,620 elements in Strut 01, 8654 in Strut 02 and 11,289 in Strut 03, giving 45,563 elements

across the support structure and 84,749 elements in the full assembly. Strut 01 carries the finest mesh of the three because it reacts the largest share of the applied load and is the strut for which damage initiation is subsequently assessed. Mesh refinement within the foil was concentrated at the cantilever end, at the mid-section, and along the leading edge between Strut 02 and Strut 03, where stress concentrations were expected. A mesh sensitivity study was carried out on the maximum normal stress in the spanwise direction under the 30% load case. The study was performed on the foil, since it is the foil that carries the strain field against which the model is assessed and the element counts quoted below refer to the foil alone. Six mesh levels were compared, with the global element size reduced from 30 to 5 mm and the element count increasing from 6424 to 39,186. The results are given in Table 3. The percentage error column reports the change in peak spanwise normal stress relative to the preceding coarser mesh. The change falls steadily from 6.82% between the 30 and 25 mm meshes to 1.83% between the 15 and 10 mm meshes, and to 1.35% between the 10 and 5 mm meshes. A convergence threshold of 2% change between successive levels was adopted. This threshold reflects the intended use of the model rather than an arbitrary numerical target. The purpose of the analysis is to reproduce the measured strain field and to locate the regions where damage initiates, and the deviations between prediction and measurement in a full-scale composite test of this type are governed by laminate variability, joint compliance, load introduction effects, and sensor placement tolerance, all of which act at the level of tens of percent. Refining the mesh below the point at which discretisation error falls to a few percent therefore adds computational cost without improving the fidelity of the comparison, since the residual difference is dominated by the physical and experimental sources rather than by the numerical solution. The 2% threshold places discretisation error an order of magnitude below those sources, which is sufficient to ensure that the mesh does not limit the conclusions drawn from the model [17,18]. The 5 mm mesh satisfies that threshold with margin and is used for all analyses reported in this paper.

Table 3: Mesh sensitivity study results.

No.	Element Size (mm)	Number of Elements	Maximum Normal Stress in Spanwise Direction (MPa)	Error (%)
01	30	6424	146.7	–
02	25	7873	156.7	6.82
03	20	8278	166.8	6.45
04	15	14,861	174.6	4.68
05	10	20,244	177.8	1.83
06	05	39,186	180.2	1.35

Subsequently, FE analysis was conducted to determine the natural frequencies of the system. The first six natural frequencies obtained from the FE model were recorded and compared against the experimentally measured values for validation purposes. Because the struts are present as deformable bodies rather than rigid restraints, the extracted modes include modes localised within the support structure in addition to the global flapwise modes of the foil. This distinction becomes relevant when the predicted modes are compared against the LSV measurements, since the observability of each mode within the scanned region governs which modes can be matched. In parallel, loadings were applied through coupling commands by distributing the loads across the modelled area to replicate the load-introducing pads used in laboratory setups. The positions of the relevant 500 and 250 kN actuators are shown in Fig. 8 labelled as ‘A’ and ‘B’, respectively. Additionally, these reference points were identified for applying these loads, aligning with laboratory conditions.

The laminate is defined as a composite layup with 34 plies in the foil skin, combining UD, BIAX, and WOVEN carbon fibre prepreg, with approximately 80% of the fibre content by mass being UD. The full stacking sequence and ply orientations are specified by ORPC Ireland and are commercially confidential, so they cannot be reproduced here. Ply material directions were mapped to a discrete orientation field following the helical surface, so that the nominal 0-degree direction tracks the local spanwise axis rather than a global datum. Laminate density was assigned so that the modelled foil mass reproduced the as-built prototype mass of 26.75 kg, and the three struts were modelled with the same shell approach using the glass fibre powder-epoxy properties against an as-built mass of 14.5 kg each. The instrumentation, the composite loading saddles, and the titanium joint hardware were not represented as discrete mass in the model. This omission introduces a known bias into the modal results, since added mass that is physically present on the article but absent from the model shifts the predicted natural frequencies upward relative to the measured values. The effect is not uniform across modes. It is most noticeable for modes whose modal displacement is largest at the locations where the unmodelled hardware is attached, which for this assembly means the cantilever tip and the strut connections. The bias is therefore carried forward as one of the candidate explanations when the matched and unmatched modes are examined later in this paper.

Loads are introduced through kinematic coupling constraints between a reference point and the surface patch representing each composite loading saddle so that the load is distributed over the same footprint as the physical saddles rather than applied at a node. The saddle geometry and its attachment to the foil are described in the companion papers on the test programme [2,8]. The mid-section patch is oriented at 40 degrees from the vertical so that the resultant acts perpendicular to the local chord, matching the wire rope and pulley arrangement described in Fig. 6. The foil-to-strut connections are hybrid bolted and bonded joints in the physical article. In the model, they are represented as tie constraints between the strut and foil surfaces, which assumes full continuity and neglects both bolt preload and adhesive compliance. This is an idealisation and is the most likely contributor to the local stiffness bias.

The boundary condition treatment requires explicit justification. All active structural degrees of freedom were restrained at the base of each of the three struts where they connect to the central shaft. In the laboratory, the struts were bolted to a steel support frame which was anchored to the reinforced concrete strong floor, so the physical restraint is stiff but not perfectly rigid. Full restraint at the strut bases is therefore an upper bound on support stiffness and the model will consequently return a stiffer global response than the article as tested. The idealisation is retained because it reproduces the intended test set. Introducing additional compliance at the supports would require the support stiffness to be inferred from the same measurements the model is being assessed against, which would convert a prediction into a fit and remove the independence of the comparison. At the same time, Simpson integration is used through the thickness with three integration points per ply, which is the Abaqus default for composite shell sections and is sufficient for the linear elastic bending response examined here. Strain was extracted at the ply mid-surface section point and the quantity reported throughout is E_{11} the logarithmic strain component in the ply local 1-direction.

Hashin's damage initiation criterion was applied to identify the regions in the composite structure where damage is likely to initiate. In this context, fibre tension, fibre compression, matrix tension and matrix compression failure criteria were analysed to identify the expected damage zones in the tidal turbine foil. Here, the investigation focused on Hashin's fibre tensile damage initiation criterion (HSNFTCRT), Hashin's fibre compressive damage initiation criterion (HSNFCCRT), Hashin's matrix tensile damage initiation criterion (HSNMTCRT) and Hashin's matrix compressive damage initiation criterion (HSNMCCRT). The mathematical formulations of the applied criteria are presented in Table 4. The Hashin criteria are used here for one purpose only, which is to establish whether the regions in which the failure indices first reach unity correspond to the regions in which damage was observed during testing. They identify

where damage is predicted to initiate. They do not simulate progressive damage evolution, post-initiation stiffness degradation, delamination, or final collapse, and no continuum damage mechanics or cohesive zone modelling was undertaken. Damage progression was outside the scope of this project, and none of the conclusions drawn in this paper depend on post-initiation behaviour.

Table 4: Hashin's damage initiation criteria and material properties [19,20].

Failure Mode	Criterion Equation	Material Properties Used
Hashin's fibre tensile damage initiation criterion (HSNFTCRT, $\sigma_{11} \geq 0$)	$\left(\frac{\sigma_{11}}{S_{t1}}\right)^2 + \left(\frac{\sigma_{12}}{S_{12}}\right)^2 \geq 1.0$	Longitudinal tensile strength S_{t1}, shear strength S_{12}, axial stress σ_{11}, shear stress σ_{12}.
Hashin's fibre compressive damage initiation criterion (HSNFCCRT, $\sigma_{11} < 0$))	$\left(\frac{\sigma_{11}}{S_{c1}}\right)^2 \geq 1.0$	Longitudinal compressive strength S_{c1}, axial stress σ_{11}.
Hashin's matrix tensile damage initiation criterion (HSNMTCRT, $\sigma_{22} \geq 0$)	$\left(\frac{\sigma_{22}}{S_{t2}}\right)^2 + \left(\frac{\sigma_{12}}{S_{12}}\right)^2 \geq 1.0$	Transverse tensile strength S_{t2}, longitudinal shear strength S_{12}, transverse stress σ_{22}, shear stress σ_{12}.
Hashin's matrix compression damage initiation criterion (HSNMTCRT, $\sigma_{22} < 0$)	$\left(\frac{\sigma_{22}}{2S_{23}}\right)^2 + \left[\left(\frac{S_{c2}}{2S_{23}}\right)^2 - 1\right] \cdot \left(\frac{\sigma_{22}}{S_{c2}}\right) + \left(\frac{\sigma_{12}}{S_{12}}\right)^2 \geq 1.0$	Transverse stress σ_{22}, transverse compressive strength S_{c2}, longitudinal shear strength S_{12}, transverse shear strength S_{23}, shear stress σ_{12}.

2.6 Material Selections for Tidal Turbine Foils

The study further focused on selecting the two most suitable UD carbon-fibre prepreg composite materials for tidal turbine foil manufacturing while keeping WOVEN and BIAX materials the same as in Table 1. Coupons cut from each prepreg system were conditioned before testing to the ASTM D3039 standard, so that the change in measured stiffness could be attributed to moisture uptake alone. This approach enabled a controlled evaluation of the effects of moisture exposure on the mechanical performance of the selected materials. For this case, UD carbon fibre prepreg composite materials manufactured by Hexcel and A&P Technology (UD-Hexcel and UD-A&P) were selected for accelerated aging, and specimens were produced. The material properties of the materials are listed in Table 5. In this case, particular attention was given to evaluating the Longitudinal Young's Modulus (E_1) and Transverse Young's Modulus (E_2); therefore, test coupons were manufactured in 0° and 90° orientations. Conditioning consisted of six months of full immersion at 50°C in order to evaluate the effects of water absorption on material degradation. The values in Table 5 are supplier datasheet properties for these two UD prepreg materials before conditioning; they serve as the baseline for comparison with the properties measured after conditioning. The A&P Poisson's ratio of 0.40 is higher than the values typically tabulated for UD carbon fibre laminates loaded in the fibre direction, which generally lie close to 0.30, and it is reported here as supplied rather than as a measured value [21,22]. The Poisson's ratio was not re-measured in the ageing programme, and the sensitivity of the FE results to it was not examined, since the strain response under the flapwise bending case reported here is dominated by the longitudinal modulus. For extracting the material properties for the conditioned and unconditioned test coupons, tensile testing was performed on a Zwick Z400 servo-controlled universal testing machine of 400 kN rated capacity with force verification in accordance with ASTM E4 as required by ASTM D3039. Coupons were tested at the standard crosshead displacement rate of 2 mm/min specified

in ASTM D3039. Nominal coupon dimensions were 250 mm in length and 25 mm in width with a cured ply thickness of approximately 2.3 mm.

Table 5: Properties of selected carbon fibre prepreg materials.

Material Type	Orthotropic Material Properties			
	E_1 (MPa)	E_2 (MPa)	G_{12} (MPa)	Poisson's Ratio
UD-Hexcel	122,230	7900	3687	0.30
UD-A&P	143,105	8860	3600	0.40

The scope of this work was limited to quantifying the effects of water absorption on material properties rather than predicting the in-service duration of degradation. Reliable time-dependent predictions require diffusion parameters and acceleration factors, particularly the diffusion coefficient governing water uptake. Furthermore, the temperature dependence of diffusion follows the Arrhenius relationship given in Eq. (1), which can be used to improve predictions of long-term water-ingression effects on composite performance [9].

$$k_d = k_0 e^{-\frac{E}{RT}} \tag{1}$$

In Eq. (1), k_0 is the reference diffusion rate, E is the activation energy, R is the universal gas constant, and T is the absolute temperature (K). The gas constant R is taken as its defined SI value of 8.3145 J/mol·K. The activation energy E is therefore expressed in J/mol, and the exponent E/RT is dimensionless as required. The diffusion coefficient k_d and the reference diffusion rate k_0 share units of mm^2/s [9]. In addition, a clear understanding of the acceleration factor is required to accurately estimate the equivalent service time represented by the accelerated aging test. The acceleration factor was estimated using Eq. (2), which follows the service-life modelling framework of Purnell et al. (2008) as applied to hygrothermal ageing by Zafari et al. (2025) [23,24]. The factor F_{HL} is dimensionless and expresses the ratio of the diffusion rate at the elevated bath temperature to that at the reference temperature. It follows directly from the ratio of Eq. (1) evaluated at the two temperatures, so the activation energy E and gas constant R carry the same units as in Eq. (1) and the bracketed term has units of reciprocal temperature. In Eq. (2), T_H and T_{Ref} are the hot bath temperature and the reference temperature, respectively [23,24]. Although vulnerability curves for tidal turbine foils can be developed by incorporating these parameters, as demonstrated through a novel methodology proposed by the University of Galway, reliable determination of the governing diffusion and acceleration parameters remains challenging [13]. Consequently, the present study aims to experimentally characterise the changes in material properties induced by water absorption and to provide preliminary design recommendations, while comprehensive service-life prediction analyses are reserved for future work. Both unconditioned and conditioned specimens were therefore prepared side by side. This paired design isolates the property changes attributable to moisture ingress alone, holding all other manufacturing and material variables fixed.

$$F_{H,L} = e^{-\left[\frac{E}{R}\left(\frac{1}{T_H}-\frac{1}{T_{ref}}\right)\right]} \tag{2}$$

3 Results and Discussion

3.1 Comparison of Strain Distribution

Under the representative loading condition corresponding to 30% of the idealised load, the 500 and 250 kN servo-hydraulic actuators recorded applied loads of 7890 N and 7360 N, respectively, under dry

laboratory conditions. These experimentally measured load values were subsequently implemented as input boundary conditions in the finite element analysis (FEA). Here, a discrepancy was observed between the estimated idealised loading and the recorded actuator loads during the static testing process. This variation can be attributed to the fact that the 250 and 500 kN servo-hydraulic actuators were designed for significantly higher load capacities than those applied in this study. The applied loads were relatively low as remaining below 8 kN during the testing phase. As a result, achieving stable and smooth load control proved challenging when using the proportional integral derivative control system integrated with the CUBUS software. The mismatch between actuator capacity and applied load range reduced control sensitivity, leading to fluctuations in the applied loading during testing. Then, the strain distribution obtained from the FEA results for the top and bottom sides of the foil was compared to the strain gauges and FBGs, and the correlations in the results were studied. Fig. 9 shows the extracted line of the strain distribution from the FE model-generated strain data according to the 30% applied loading conditions.

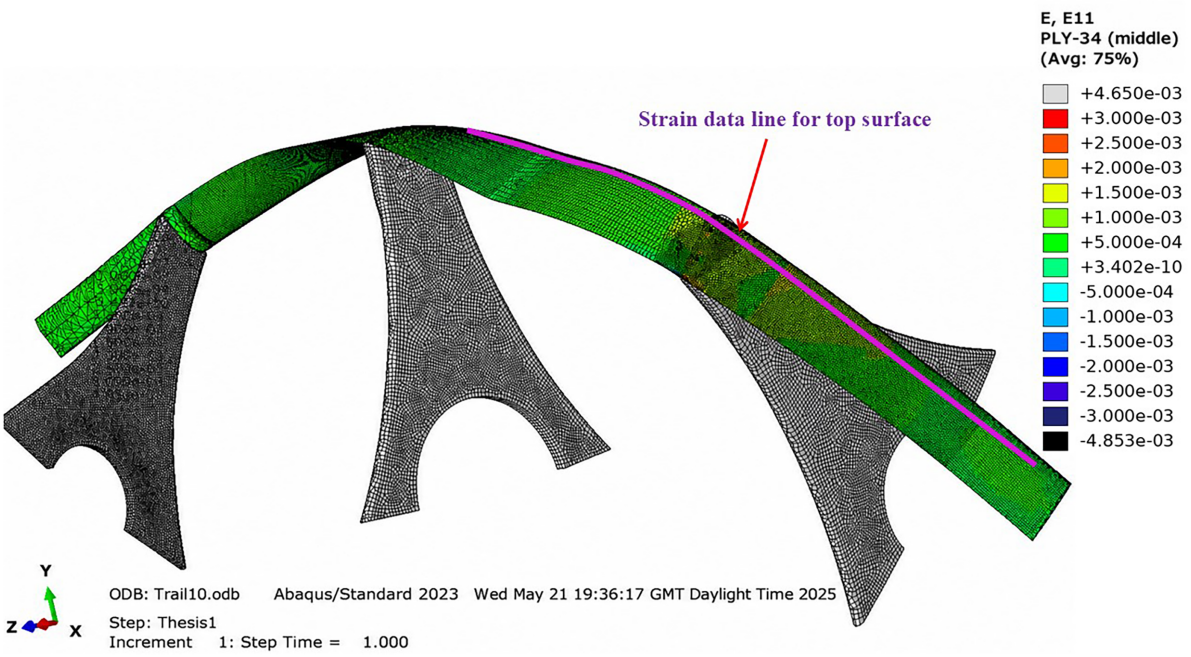


Figure 9: FE-predicted spanwise strain distribution along the extraction path.

The quantity plotted in Fig. 9 is E_{11} FE-predicted spanwise strain distribution along the extraction path and it is the logarithmic strain component in the ply local 1-direction expressed in microstrain. Values are taken at ply 34 of the laminate at the mid-surface section point without nodal averaging across adjacent elements. Labels A and B in the figure mark the load introduction reference points for the 500 and 250 kN actuators, respectively, as defined in Fig. 6. Fig. 10 displays the strain distribution comparison with reference to the strain gauges, FBG sensors, and FE model-generated results, and the horizontal axis is the spanwise coordinate measured from the cantilever tip and increasing towards Strut 03. Here, it is possible to observe correlations between experimental and FEA results as the patterns of the strain distribution are similar to each other. However, discrepancies are observed in various regions of the foil when comparing the experimental strain data with the FE model results. At the cantilever's fixed end, top surface FBG data showed a maximum deviation of approximately 28% from the FEA results, while strain gauges exhibited a larger deviation of 45%, as shown in Fig. 10. Notably, the deviations on the top surface were minimal (within 10%) in other regions, such as near the cantilever tip and Strut 02.

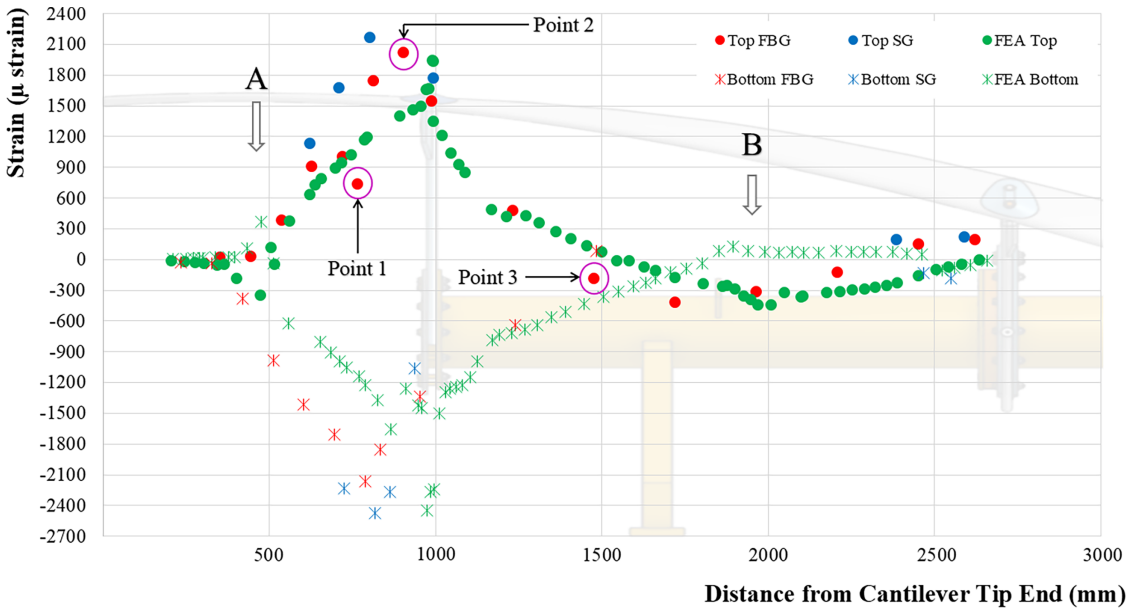


Figure 10: Measured and FE-predicted spanwise strain under the 30% idealised load case.

A direct comparison against the earlier model of this foil is instructive. The initial FE model reported for this structure represented the foil alone with all active structural degrees of freedom restrained at the three strut positions [2]. In the present model, the three glass fibre struts are resolved as discrete structural bodies, so that the load path through the support structure is carried explicitly rather than terminated at an idealised restraint. The consequence is confined to the cantilever fixed end but is substantial there. The predicted peak spanwise strain in that region rises from approximately 1519 microstrain in the foil-only model to approximately 1934 microstrain when the struts are included, bringing the prediction considerably closer to the 2015 microstrain recorded by the FBG sensor at 905 mm and the 2161 microstrain recorded by the strain gauge at 802 mm.

Away from the fixed end, the two models are indistinguishable, which localises the effect to the region where the support idealisation acts. This is the central numerical result of the present study. It demonstrates that the deviations previously attributed in part to simplified boundary conditions were, in that region, a consequence of the support representation rather than of the laminate definition or the load introduction, and it establishes that explicit modelling of the support structure is required for a foil of this construction if the strain field near the strut connections is to be predicted with confidence. The strain recorded by the FBG sensors at “Point 1”, “Point 2”, and “Point 3” shows spatial deviations from the corresponding results generated by the FE model. Similarly, certain strain gauge and FBG data points show comparable deviations, though these are only partially captured by the FE model predictions. Nonetheless, the overall trend of the FBG measurements aligns well with the pattern predicted by the FE model. Moreover, no experimental data are available near the foil-to-Strut 01 hybrid composite joint due to the obstruction caused by a 3D-printed titanium pad, which restricts sensor placement. In this context, it is challenging to correlate the strain distribution close to the hybrid composite joint. These observations generally also apply to the bottom surface of the foil with only minor variations. Furthermore, all these discrepancies may also be influenced by parasitic effects at the load introduction points, as noted in a study conducted by the University of Edinburgh [10]. Additionally, localised stress concentrations near the fixed end of the cantilevered tidal turbine foil, along with simplified boundary conditions and loading assumptions during the FEA modelling process, likely contributed to these significant deviations between the FEA and experimental results. Overall, the agreement can be highlighted as follows.

- Cantilever fixed end, top surface: approximately 28% maximum deviation for FBG channels, and 45% for strain gauge channels.
- Near the cantilever tip and around Strut 02: within approximately 10%.
- Bottom surface: same pattern as the top surface.

Against the bands defined above, the fixed-end channels fall in the poor band, the transition region between the fixed end and Strut 02 falls in the acceptable band, and the remainder fall in the good band. The close agreement between the two property sets indicates that the deviation is not principally driven by the choice of input properties. The distribution of that deviation matters more than its magnitude. The poor-band channels are not scattered along the span. They cluster at the fixed end where the largest strain gradients occur and where the load introduction saddle, the hybrid bolted and bonded joint, and the strut restraint are concentrated within a short length. Four mechanisms are consistent with that pattern.

- The full restraint applied at the struts is stiffer than the physical support frame, suppressing local compliance exactly where the largest deviations occur.
- The tie constraint at the foil-to-strut joint neglects adhesive shear compliance and bolt preload, acting in the same direction.
- Parasitic strain fields near load introduction points add a disturbance that a shell model with idealised coupling cannot capture.
- Reduced load control resolution from operating 500 and 250 kN actuators below 8 kN introduces scatter in the applied load that propagates into the measured strain.

Separating these contributions would require a strain survey at closer spacing through the strut region than the present instrumentation provides, together with an instrumented joint, and is recommended for future campaigns rather than resolved here. Deviations of this order are not anomalous for full-scale composite blade tests, with comparable studies reporting the largest discrepancies near the fixed boundary and at load introduction points [6,10]. What differs here is that the crossflow architecture places three hybrid bolted and bonded strut connections along the span rather than a single root boundary, so the region over which support idealisation degrades the prediction appears at three stations rather than one. This argues for joint-level characterisation as the next step rather than further refinement of the global shell model. Global displacement provides a complement to the local strain data. Under the 30% load case, the cantilever tip deflected 52 mm while the higher middle section deflected 9 mm, and the FE model reproduces the same deflected shape and stiffness ordering.

3.2 Comparison of Dynamic Results

The LSV system recorded the dynamic response before applying the 30% idealized loading on the tidal turbine foil; the resulting first mode shape is illustrated using 21 scanning points in Fig. 11. The recorded natural frequencies in this case were 23.88, 37.50, and 62.75 Hz, respectively. Fig. 11b visualised the LSV-generated first mode shape related to 21 scanning points. At the same time, the results of the dynamic analysis performed using the FE model are presented in Fig. 12, which illustrates the first six mode shapes of the system. Here, the displacement magnitudes reported in each contour legend follow from the mass normalisation applied during eigenvalue extraction and carry no physical amplitude. Only the mode shape and the associated natural frequency are meaningful. The contour range and the deformation scale factor therefore differ between panels and are not comparable across modes. The corresponding natural frequencies obtained from the FE simulation are 24.24, 24.52, 25.46, 25.47, 52.59, and 63.47 Hz. These frequencies represent the system's primary vibrational modes as predicted under idealised boundary and material conditions. For experimental validation, LSV recorded three prominent natural frequencies at 23.88, 37.50, and 62.75 Hz. The first (24.24 Hz) and sixth (63.47 Hz) modes predicted by the FE model show good

correlation with the first and third experimental modes, respectively, indicating partial agreement between simulation and testing. However, the intermediate experimental frequency at 37.50 Hz does not correspond to any clearly isolated mode in the FE results. Additionally, the FE simulation predicted four closely spaced modes between 24.24 and 25.47 Hz, each with distinct mode shapes as shown in Fig. 12. Since the mode shapes at 25.46 and 25.47 Hz (modes 3 and 4) are local in nature, as shown in Fig. 12, they are unlikely to be captured by the LSV measurement and may therefore be excluded from the comparison. The absence of a clear match for the 37.50 Hz experimental mode may also stem from modelling simplifications such as idealised boundary constraints, omission of damping, or unmodelled structural interfaces. Thus, while the FE analysis provides valuable insight into the system's modal characteristics, it does not fully replicate the experimentally observed dynamic response.

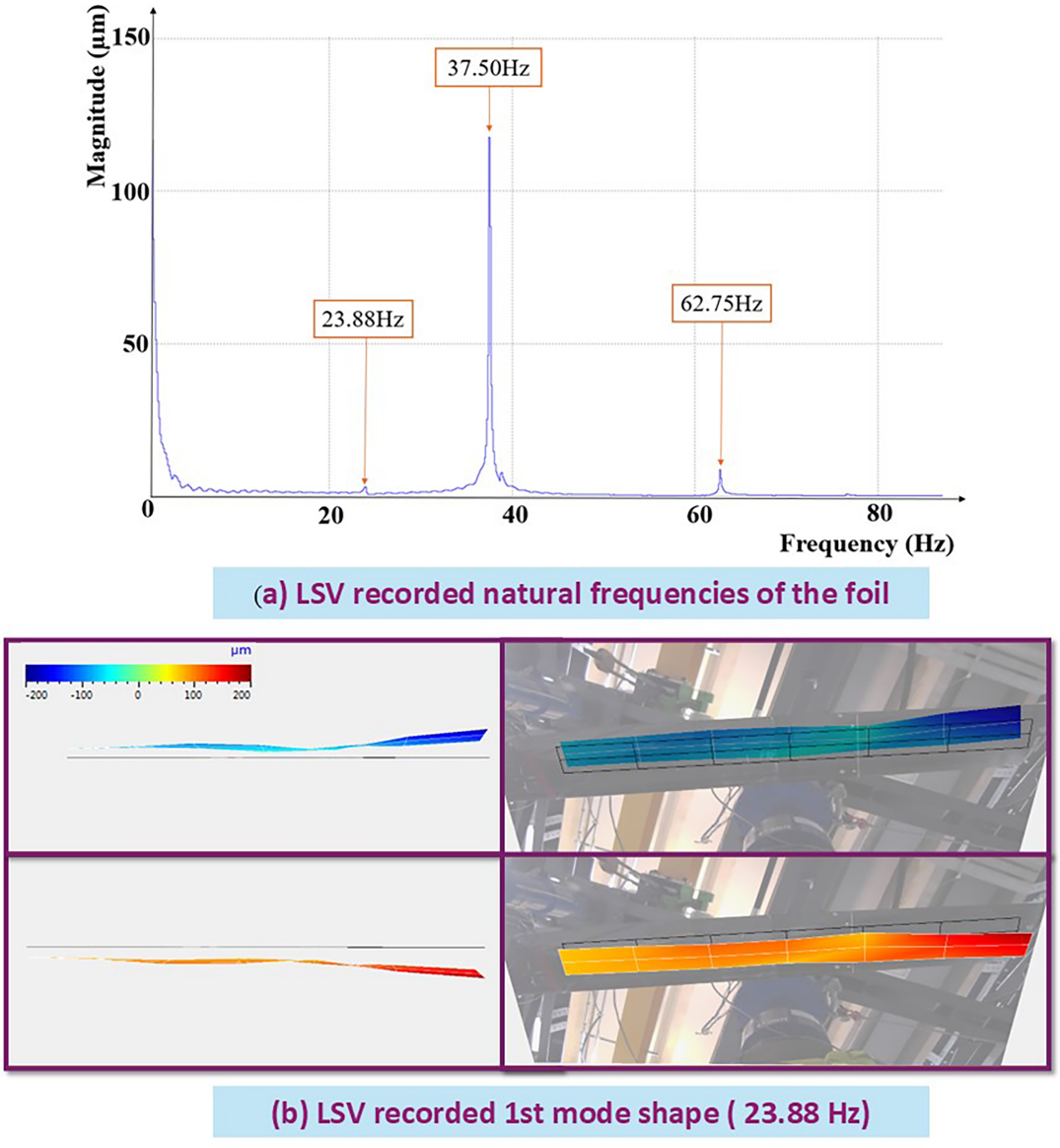


Figure 11: LSV recorded natural frequencies and 1st mode shape of the foil [2].

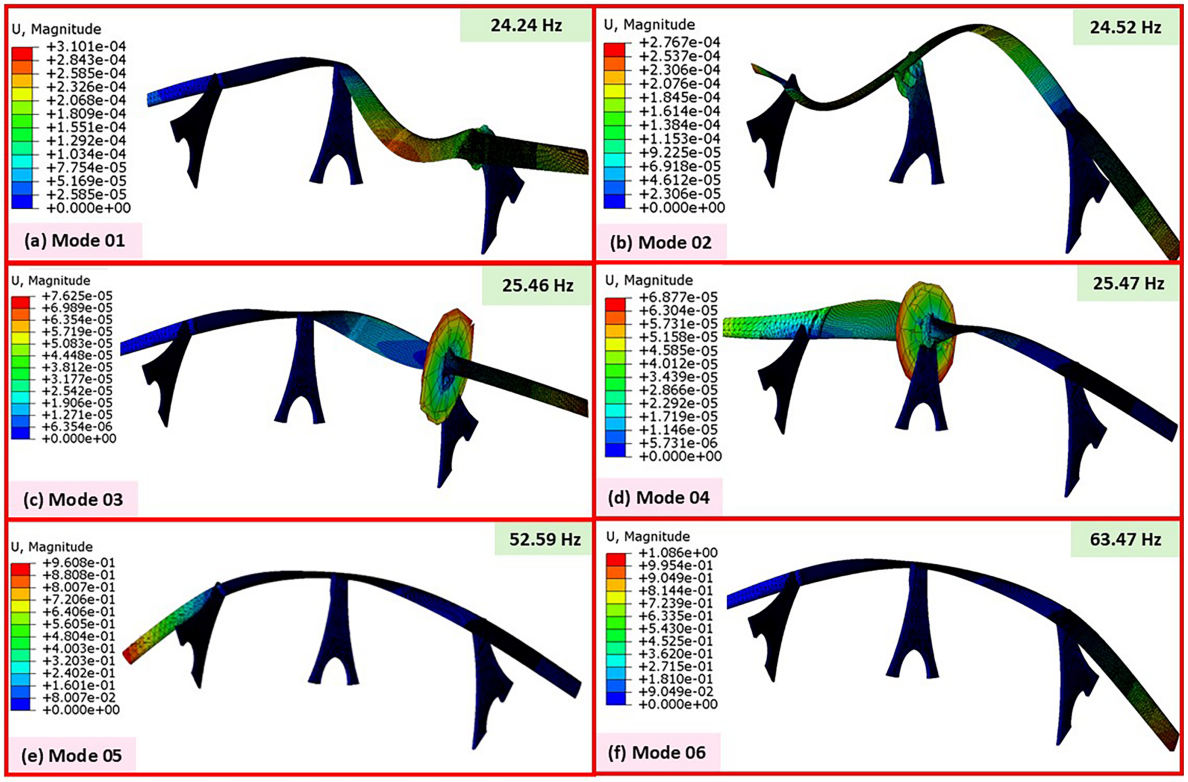


Figure 12: FE-predicted mode shapes of the foil and strut assembly.

Observability is the governing limitation in this comparison. The 21 scan points cover a rectangular patch on the bottom surface of the cantilever section only, and the full sensor and scanning arrangement is documented in the companion paper on measurement techniques [8]. Any mode whose modal displacement is small within that patch will be weakly represented in the measured spectrum regardless of how strongly it participates globally. This is the basis on which FE modes 3 and 4, at 25.46 and 25.47 Hz, are set aside. Inspection of the predicted mode shapes shows that both are localised in the strut assembly and in the region between Strut 02 and Strut 03 with negligible modal displacement over the scanned patch, so their absence from the measured spectrum is expected rather than anomalous. The same reasoning does not extend to the predicted mode at 52.59 Hz, which does involve motion of the cantilever section, and its absence from the measurement is treated below as an open discrepancy. More generally, because the LSV scanned only the cantilevered portion of the foil, modes occurring predominantly within the other three segments could not be identified accurately. The limited density of the 21 scan points may also have prevented the LSV from resolving local modes with highly localised deformation. The FE model therefore predicts more modes than the experimental survey was able to capture, and this reflects the coverage of the measurement rather than a deficiency in the model.

Frequency agreement alone is not sufficient evidence of mode pairing, since two dissimilar mode shapes can coincide in frequency. For the two matched pairs, the LSV-generated mode shapes were therefore compared visually against the corresponding FE mode shapes, and both were confirmed as first and higher-order global flapwise bending of the cantilever section with the node positions falling in the same locations along the span. This is a qualitative confirmation of the pairing rather than a quantitative one. A formal correlation using the modal assurance criterion would require the FE mode shapes to be mapped onto the

21 scan-point coordinates and would provide a defensible numerical measure of shape agreement. That was not undertaken in this study, and it can be identified as future work.

The frequency agreement for the two matched pairs is close. Mode 1 differs by 0.36 Hz, or 1.51%, and the higher global mode differs by 0.72 Hz, or 1.15%. Across the matched pair, the mean absolute error is 0.54 Hz, the root mean square error is 0.57 Hz, and the mean absolute percentage error is 1.33%. Two discrepancies remain unresolved and are stated as such. The experimental mode at 37.50 Hz has no FE counterpart at any proximity, and the predicted mode at 52.59 Hz was not identified in the measured spectrum. Several mechanisms could account for the unmatched experimental mode. The tie constraint at the foil-to-strut joints removes a compliance that would lower a coupled joint mode into that range. Damping was not included in the extraction, so modes that are heavily damped in the article appear undamped in the model. The mass of the loading pads, titanium joint hardware, and installed instrumentation was not represented, and added mass shifts frequencies downward in a way the model cannot reproduce. The support frame itself was not modelled, so any frame-foil interaction mode is absent by construction. Resolving which of these dominates requires a modal survey over the full structure rather than the cantilever patch, and that is left to future work. A detailed summary of the discussion related to the LSV recorded and FE-modelled frequencies is given in Table 6.

Table 6: Comparison of LSV measured and FE-predicted natural frequencies.

LSV Recorded Mode	LSV Frequency (Hz)	Corresponding FE Mode	FE Frequency (Hz)	Difference (%)	Remarks
Mode 1	23.88	Mode 1	24.24	1.5	Excellent agreement; global mode captured accurately by FE model.
–	–	Mode 2	24.52	–	Closely spaced mode predicted by FE model; not distinctly identified in LSV measurements.
–	–	Mode 3	25.46	–	Local mode shape; unlikely to be detected by LSV due to limited global response.
–	–	Mode 4	25.47	–	Local mode shape; excluded from direct comparison with experimental results.
Mode 2	37.5	–	–	–	No clearly corresponding FE mode identified; may result from modelling simplifications, boundary-condition uncertainties, or mode coupling effects.
–	–	Mode 5	52.59	–	Predicted by FE model but not observed experimentally.
Mode 3	62.75	Mode 6	63.47	1.1	Very good agreement; FE model accurately predicts higher-order global mode.

3.3 Study of Damage Initiation Criteria

During the final static test, the tidal turbine foil was subjected to 110% of the idealised design load, leading to the initiation of structural damage. The experimental observations were subsequently compared with FE predictions to evaluate the model's ability to identify the start of failure. For this purpose, the FE analysis was expanded to include a damage initiation assessment of the complete structure comprising the

foil and its three supporting struts, as shown in Fig. 13. The damage initiation of Strut 01 occurs due to the compression and the Fig. 13a and b illustrate the regions predicted for fibre and matrix material damage initiations due to the compression loading, respectively. Under compressive loading, powder epoxy glass fibre composites often exhibit matrix cracking, fibre-matrix debonding, and micro buckling of fibres, leading to fragmentation of the brittle epoxy matrix and the release of fine, powder-like debris as a characteristic damage byproduct, as shown in Fig. 13c. Subsequently, to identify the initiation of damage in the tidal turbine foil, the study was focused solely on the foil, as shown in Fig. 14. The analysis indicated that damage initiation could occur at both the trailing and leading edges as well as along the connection region between the foil and Strut 01 on the outboard side. In this context, as highlighted by Hashin's damage initiation criteria, damage at the trailing and leading edges was observed under dry laboratory conditions as illustrated in Fig. 15.

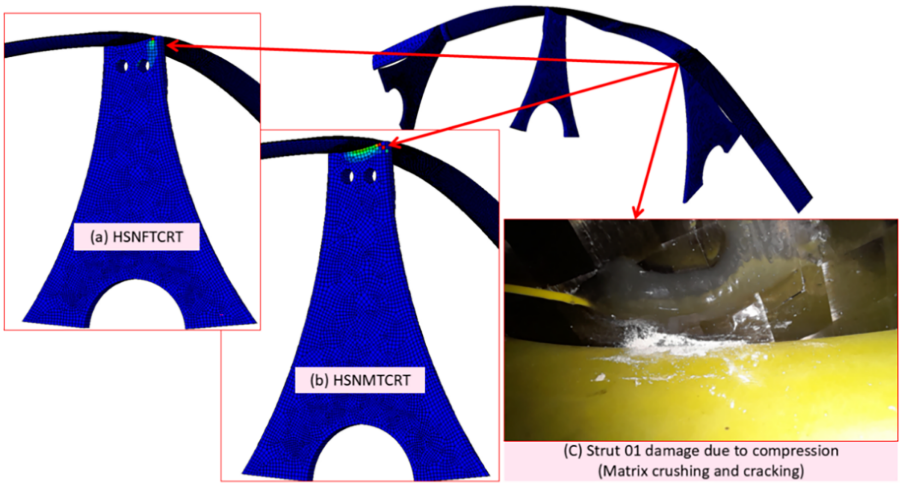


Figure 13: FE model generated damage initiation criteria for strut 01.

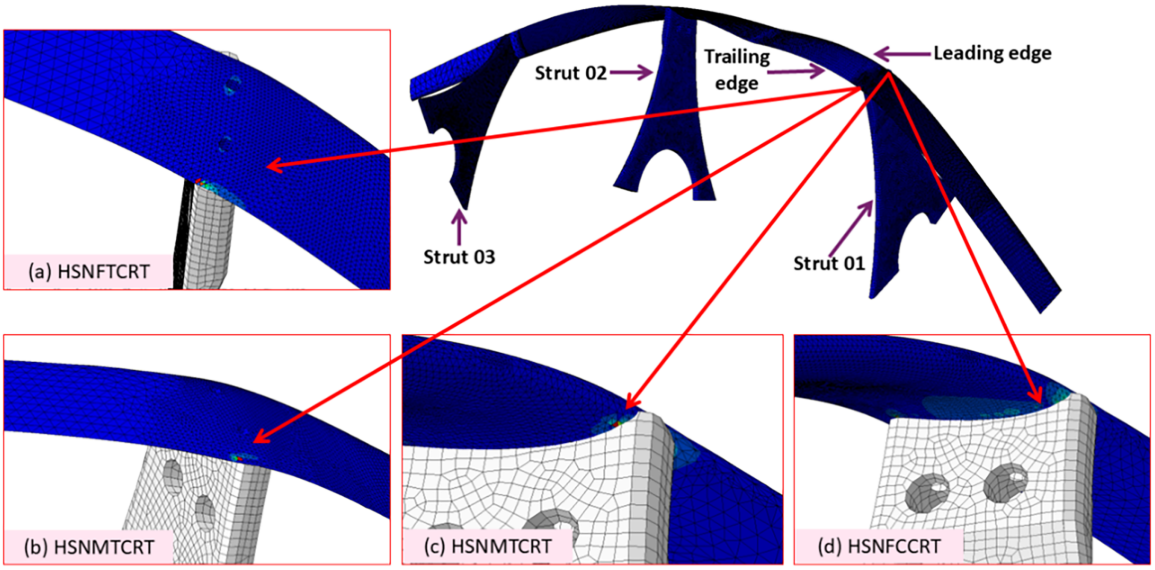


Figure 14: FE model generated damage initiation criteria for foil.

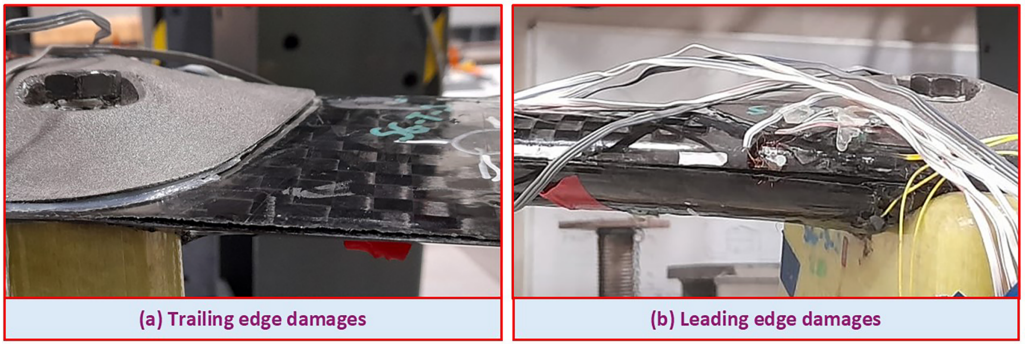


Figure 15: Leading and trailing edge damage.

The predicted failure indices first reach unity at the same leading and trailing edge locations where damage was recorded at the final test stage, and at the cantilever fixed end near the connection to Strut 01. That correspondence indicates the model reproduces the load path and the distribution of critical regions correctly, which is the minimum requirement for a model intended to support design decisions. It is a check on where the structure is most highly loaded, not on the individual modelling inputs, and it does not establish the accuracy of the predicted initiation load. The experimental record captures damage visible at the conclusion of the 110% load case rather than the load at which damage first appeared, so no measured onset exists for comparison, and damage progression was outside the scope of this project.

3.4 Comparison of Strain Distribution with Aged Materials Properties

The tensile testing was performed in accordance with ASTM D3039 for the coupons prepared using Hexcel and A&P UD carbon-fibre prepreg materials, which were unconditioned and subjected to accelerated aging. Fig. 16 presents the accelerated aging and tensile testing setup for the coupons used to determine the longitudinal modulus (E_1).

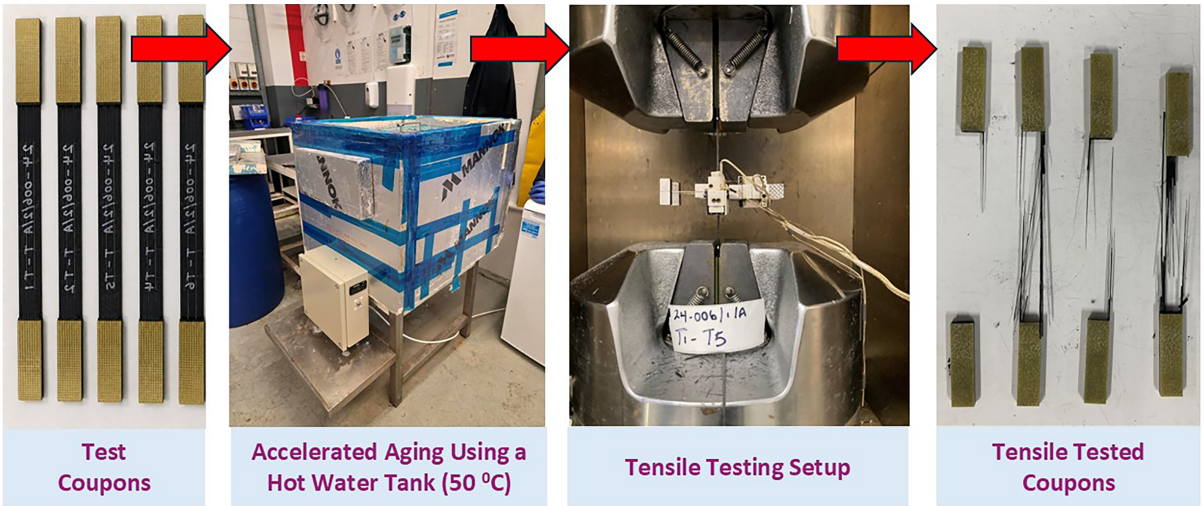


Figure 16: Accelerated aging and tensile testing setup.

Table 7 summarises the extracted material properties and compares unconditioned coupons with coupons conditioned by six months of full immersion in water held at 50°C. No equivalent in-service

duration is assigned to that condition. As set out there, converting accelerated immersion condition into a service-life equivalent requires the diffusion coefficient for this laminate, the activation energy for the diffusion process, a verified acceleration factor and a demonstrated saturation criterion, none of which were determined in this study. The conditioned results are therefore reported as the measured response after a defined laboratory exposure, and not as a service-life prediction.

Table 7: Derived material properties.

Material	Properties for Unconditioned		Properties for Conditioned	
	E_1 (MPa)	E_2 (MPa)	E_1 (MPa)	E_2 (MPa)
Hexcel	127,590	7660	130,110	7200
A&P	150,590	8729	147,520	8310

The in-plane shear modulus (G_{12}), longitudinal through-thickness shear modulus (G_{13}), and transverse through-thickness shear modulus (G_{23}) were taken from the manufacturer's datasheet, as listed in Table 5, since these properties were not determined experimentally. The measured longitudinal and transverse moduli for the unconditioned and conditioned states were then propagated through the model of the full foil and strut assembly by giving the top surface only comparative results shown in Fig. 17, where the red curves correspond to the UD Hexcel foil and the blue curves to the UD A&P foil. These results were first reported in the assessment of these two material systems presented at OMAE 2026 and are included here so that the ageing behaviour can be considered alongside the modal correlation and damage initiation analyses reported in this paper [25]. Table 7 shows that the conditioned Hexcel coupons return a higher E_1 than the unconditioned specimens, which runs counter to the stiffness reduction expected from moisture-induced matrix plasticisation. Several mechanisms could account for this, including batch-level statistical variability, local variation in fibre volume fraction or laminate thickness, and post-curing during the conditioning period, which can introduce additional crosslinking and raise the measured modulus values [26,27]. The present dataset cannot distinguish between them. The measured difference is 1.97%, which is within the scatter that any of these mechanisms could produce across two small coupon batches, and specimen-level standard deviations were not recorded. The result is therefore retained and reported as an open question rather than resolved.

The FE model results presented in Fig. 17 indicate that the overall strain distributions along the tidal turbine foil span do not differ substantially between data-sheet values, unconditioned properties and conditioned properties. The conditioned Hexcel result is retained and reported rather than discarded. Excluding a measurement because it runs against expectations is not defensible, and the result carries information about the uncertainty of the programme. Measured against the unconditioned state, conditioned Hexcel shows a 1.97% increase in longitudinal modulus and a 6.01% reduction in transverse modulus, while conditioned A&P shows a 2.04% reduction in longitudinal modulus and a 4.80% reduction in transverse modulus. The transverse response is consistent in sign across both materials, which is what matrix-dominated moisture degradation would produce, and its magnitude is the larger of the two effects in both systems. The longitudinal response is not consistent in sign, and for Hexcel it moves in the direction opposite to the expected trend. Whether that increase is real cannot be resolved with the present dataset, since the scatter of the coupon population was not recorded and a 1.97% shift is well within the variability that post-curing, local fibre volume fraction variation and specimen handling could produce between two small batches. The A&P dataset is used as the primary basis for the FE degradation study because its behaviour is

internally consistent across both moduli, but the Hexcel result is carried forward as an open question rather than removed.

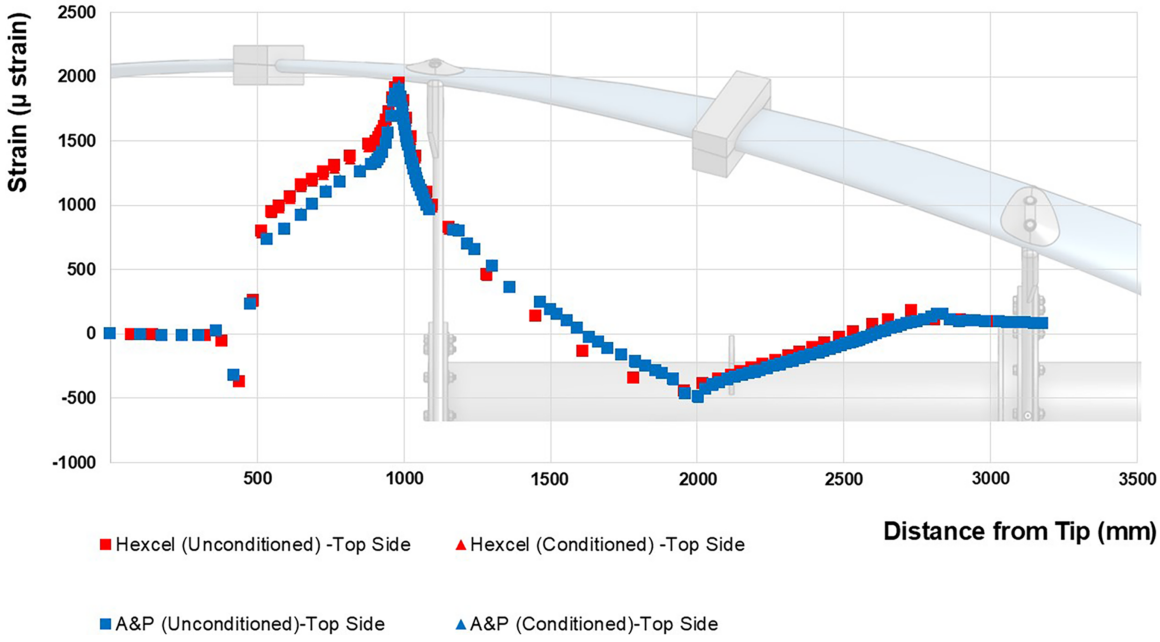


Figure 17: Predicted top surface spanwise strain for unconditioned and conditioned coupon properties.

The A&P material shows internally consistent behaviour across both moduli, and propagating its conditioned properties through the FE model produces an increase in predicted strain of approximately 2% relative to the unconditioned case. Whether that increase is meaningful depends on how it compares with the uncertainty in the chain that produced it. The model-to-experiment deviation reported reaches 28% for the FBG channels and 45% for the strain gauges at the cantilever fixed end, and the coupon scatter for the conditioning programme was not quantified. A 2% shift is an order of magnitude smaller than the model error and cannot be separated from coupon variability on the present evidence. It is therefore reported as a preliminary indication of the direction of change and not as a quantified degradation rate. The value of the result lies in the sign and the ordering, which show the transverse, matrix-dominated response degrading more than the longitudinal, fibre-dominated response exactly as moisture ingress into the matrix would predict. The associated reduction in stiffness is small. However, it could in principle accelerate fatigue damage accumulation by increasing local cyclic strains, thereby promoting matrix cracking, fibre-matrix debonding, and delamination under long-term tidal loading. This trend confirms that water absorption degrades the mechanical performance of composite structures. The extent of that degradation depends strongly on the material system, the resin chemistry and the laminate configuration. Such sensitivity highlights the need for material-specific moisture diffusion models and long-term durability characterisation when designing tidal turbine foils for marine environments. The combined FE-experimental approach used here offers a practical route for evaluating moisture-induced degradation in carbon-fibre prepreg tidal turbine foils. Prior marine durability studies have relied mainly on dry testing or small-scale laboratory specimens, and this work moves beyond both.

The basis for comparing the two materials is narrower than a manufacturing decision requires, and the conclusion is framed accordingly. Only the longitudinal and transverse moduli were measured in this programme. The shear moduli were taken from supplier datasheets and were not measured for either

material in either condition. No comparison was made of tensile or compressive strength, in-plane shear strength, fracture toughness, fatigue performance, water uptake rate, manufacturability or cost. What the present dataset supports is the following. Within this limited property set, A&P showed the more internally consistent modulus response to conditioning, with both moduli moving in the direction expected for moisture ingress, whereas Hexcel did not. That is a reason to carry A&P forward as the leading candidate for further characterisation. It is not sufficient to identify A&P as the more reliable material for turbine foil manufacture, and no such claim is made here. Future work should evaluate fatigue performance alongside other key material properties. That includes tensile and compressive strength, in-plane shear strength, flexural strength, fibre volume fraction and glass transition temperature. Nevertheless, mechanical performance alone cannot settle the material choice. A full techno-economic evaluation is needed first, weighing cost, manufacturability, supply chain stability and processing requirements, factors that carry just as much weight for large-scale tidal energy deployment. Future research should therefore fold in economic analysis, staged multi-level ageing studies and laminate-level optimisation. Degradation should be tracked at 5, 10, 15 and 20 year equivalent exposure levels, giving a clearer picture of long-term service conditions. Moisture uptake in operational turbines is also shaped by rotational hydrodynamic loading. Accelerated ageing protocols should therefore fold in cyclic pressure and flow conditions, so the induced moisture diffusion and mechanical degradation better match what the blade sees in service.

4 Conclusion

This study developed an FE model of a full-scale 5 m helical crossflow tidal turbine foil and correlated it against static strain, modal and damage observations from a full-scale test campaign. The model was then used to propagate conditioned and unconditioned coupon properties for two carbon fibre prepreg systems. The principal findings are as follows.

- The model reproduces the spanwise strain distribution well over most of the foil, with normalised errors within approximately 10% away from the support region. Agreement is poor in a bounded region at the fixed end of the cantilever, where deviations reach approximately 28% for the FBG channels and approximately 45% for the strain-gauge channels. The encastre boundary condition at the three struts, the tie treatment of the hybrid bolted and bonded joints, and parasitic effects at the load introduction points are the mechanisms consistent with that pattern.
- Modal correlation is partial rather than complete. Two of six predicted modes are corroborated by LSV measurement, at 1.51% and 1.15% frequency difference. One measured mode at 37.50 Hz has no FE counterpart, and one predicted mode at 52.59 Hz was not observed within the scanned region. The model is a reliable predictor of the first and highest global flapwise modes of this assembly. It has not yet been demonstrated for the intermediate modal content.
- Predicted damage initiation zones at the leading and trailing edges and at the cantilever fixed end near Strut 01 coincide spatially with the damage recorded at the final test stage. This was the intended outcome of the damage analysis and confirms that the load path and laminate definition are reproduced correctly. Damage progression was outside the scope of this work and initiation load accuracy was not verified, so the claim is limited to spatial consistency.
- Six months of immersion at 50°C produced a reduction in transverse modulus in both prepreg systems, together with an inconsistent longitudinal response. Propagated through the FE model, the A&P-conditioned properties give an increase in predicted strain of approximately 2%. That shift is small relative to the model-to-experiment error established in this study, and it is reported as a preliminary indication of direction rather than a quantified degradation rate. No service-life equivalent is assigned to the conditioning.

- Within the limited property set measured here, A&P showed the more internally consistent modulus response to conditioning and is carried forward as the leading candidate for further characterisation. Material selection for manufacture requires strength, fatigue, fracture, water uptake, manufacturability and cost data that this programme did not generate.
- The FE work was scoped to a single representative static case at 30% of the idealised load together with modal and damage initiation assessment. Fatigue and cyclic load cases were not modelled. Taken together, the static, dynamic and damage initiation correlations establish that the model reproduces the elastic response, the global modal content and the distribution of critical regions in the as-built article, which is the necessary foundation before fatigue and operational load spectra are introduced. A model of this type can reduce the number of full-scale tests required during development and can target where instrumentation and inspection effort is best placed. It is not offered as a substitute for structural qualification testing.

Priorities for future work follow directly from these limitations. A full-structure modal survey with quantitative mode-shape correlation, using the modal assurance criterion, would resolve the unmatched modes. Instrumented onset detection during loading would convert the spatial damage agreement into quantitative initiation validation, and progressive damage modelling would extend the analysis beyond initiation. Multi-stage conditioning with monitored moisture uptake and reported coupon scatter would place the ageing results on a statistical footing. Extending the model to cyclic and fatigue load cases remains the principal step between the present correlation and confidence in long-term operational performance.

Acknowledgement: We would like to acknowledge the support from Construct Innovate and the Ryan Institute, and the technical staff at the University of Galway, along with appreciation for the invaluable support extended by the industry partners, ORPC, CTL and ÉireComposites.

Funding Statement: This work was funded by the European Commission under the H2020 CRIMSON project, Grant Agreement no. 971209, received by T. F., C. C., P. C. and W. F. (https://cordis.europa.eu/project/id/971209); by the TIDAL-GES project of the University of Galway Global Challenges Programme, received by T. R. M. T., W. F. and J. G. (https://www.universityofgalway.ie); by the MaREI Research Ireland Centre for Energy, Climate and Marine, funded by Taighde Éireann-Research Ireland, formerly Science Foundation Ireland, under Grant no. 12/RC/2302_2, received by J. G. and W. F. (https://www.researchireland.ie); by the Sustainable Energy Authority of Ireland under Grant nos. 22/RDD/783, 23/RDD/917 and 23/RDD/1021, received by W. F. and J. G. (https://www.seai.ie); and by the Marine Institute under the Marine Research Programme of the Government of Ireland, Grant no. PDOC/21/03/01, received by W. F. (https://www.marine.ie). The initials refer to T. Flanagan (T. F.), C. Courade (C. C.), P. Cronin (P. C.), J. Goggins (J. G.), T. R. Munaweera Thanthirige (T. R. M. T.) and W. Finnegan (W. F.).

Author Contributions: The authors confirm contribution to the paper as follows: study conception and design: Tenis Ranjan Munaweera Thanthirige, Jamie Goggins, William Finnegan; design, manufacture and supply of the test article: Tomas Flanagan, Micheal O'Conghaile, Clement Courade, Conor Dillon, Patrick Cronin; full-scale structural test programme, instrumentation and data collection: Tenis Ranjan Munaweera Thanthirige, Michael Flanagan, Ciaran Kennedy, Yadong Jiang; accelerated ageing and coupon characterisation: Jeffwin George, Michael Walls; finite element model development and simulation: Tenis Ranjan Munaweera Thanthirige, Yadong Jiang, William Finnegan; analysis and interpretation of results: Tenis Ranjan Munaweera Thanthirige, Michael Flanagan, Yadong Jiang, Edward M. Fagan, Jamie Goggins, William Finnegan; draft manuscript preparation: Tenis Ranjan Munaweera Thanthirige; manuscript review and editing: Michael Flanagan, Ciaran Kennedy, Yadong Jiang, Michael Walls, Patrick Cronin, Edward M. Fagan, Jamie Goggins, William Finnegan; project administration and funding acquisition: Tomas Flanagan, Micheal O'Conghaile, Clement Courade, Patrick Cronin, Jamie Goggins, William Finnegan; supervision: Jamie Goggins, William Finnegan. All authors reviewed and approved the final version of the manuscript.

Availability of Data and Materials: The data supporting the findings of this study are available from the corresponding author on reasonable request. Full laminate geometry and stacking sequence details are the property of ORPC Ireland and are subject to commercial confidentiality. Notwithstanding that restriction, the following are available on request: normalised sensor coordinates for all strain-gauge and FBG channels, processed strain data averaged over the three load ramps with associated scatter, the LSV frequency response functions and identified mode shapes at the 21 scan points, the coupon-level tensile data for both prepreg systems in both conditions, and a modelling workflow description sufficient to reproduce the analysis from an equivalent laminate definition.

Ethics Approval: Not applicable. This study did not involve human participants, human tissue or animal subjects. The work comprised full-scale structural testing of a composite tidal turbine foil, coupon level material characterisation and finite element modelling, and therefore no ethical approval, institutional review board approval or registration identifier was required.

Conflicts of Interest: Authors affiliated with ORPC Ireland and ÉireComposites Teo have a commercial interest in the tidal turbine system that is the subject of this study. The experimental testing, FE modelling and data interpretation were carried out by the University of Galway authors. The industry partners supplied the test article, the laminate specification, and the design load case. The authors declare no other competing interests.

Notation

E_1, E_2	Young's modulus
F_{HL}	Acceleration factor between hot-bath and reference temperature
G_{12}, G_{13}, G_{23}	In-plane and through-thickness shear moduli (MPa)
HSNFTCRT	Hashin fibre tensile damage initiation criterion (Abaqus output label)
HSNFCCRT	Hashin fibre compressive damage initiation criterion (Abaqus output label)
HSNMTCRT	Hashin matrix tensile damage initiation criterion (Abaqus output label)
HSNMCCRT	Hashin matrix compressive damage initiation criterion (Abaqus output label)
k_d	Diffusion coefficient governing water uptake
k_0	Reference diffusion rate
LCOE	Levelised cost of energy
LSV	Laser scanning vibrometer
MAC	Modal assurance criterion
MAE	Mean absolute error
R	Universal gas constant (8.3145 J/mol·K)
RMSE	Root mean square error
S_{c1}, S_{c2}	Longitudinal and transverse compressive strength (MPa)
S_{t1}, S_{t2}	Longitudinal and transverse tensile strength (MPa)
S_{12}, S_{23}	Longitudinal and transverse shear strength (MPa)
T	Absolute temperature (K)
T_H, T_{ref}	Hot-bath and reference temperature (K)
TEC	Tidal energy converter
UD	Unidirectional carbon fibre prepreg reinforcement
σ_{11}, σ_{22}	Longitudinal and transverse normal stress (MPa)
σ_{12}	In-plane shear stress (MPa)

References

1. Shyamala G, Ravindran G, Alaneme GU, TR, Dhanapalan S. Harnessing the future of renewable energy: integrated insights of ocean energy. Energy Nexus. 2026;21(8):100622. doi:10.1016/j.nexus.2025.100622.
2. Munaweera Thanthirige TR, Flanagan M, Kennedy C, Jiang Y, O'Conghaile M, Courade C, et al. Advanced structural testing and modelling of a novel full-scale helical shape tidal turbine foil. Eng Struct. 2025;330:119864.

3. Walker S, Thies PR. A review of component and system reliability in tidal turbine deployments. Renew Sustain Energy Rev. 2021;151(12):111495. doi:10.1016/j.rser.2021.111495.
4. DNV-ST-0164. Tidal turbines. Høvik, Norway: Det Norske Veritas; 2015.
5. IEC TS 62600–3:2020. Geneva, Switzerland: International Electrotechnical Commission; 2019.
6. Finnegan W, Jiang Y, Meier P, Hung LC, Fagan E, Wallace F, et al. Numerical modelling, manufacture and structural testing of a full-scale 1 MW tidal turbine blade. Ocean Eng. 2022;266(5):112717. doi:10.1016/j.oceaneng.2022.112717.
7. Leon-Medina JX, Tibaduiza DA, Parés N, Pozo F. Digital twin technology in wind turbine components: a review. Intell Syst Appl. 2025;26(8):200535. doi:10.1016/j.iswa.2025.200535.
8. Munaweera Thanthirige TR, Flanagan M, Kennedy C, Jiang Y, Courade C, Cronin P, et al. Advanced measuring techniques for tidal turbine blades during structural testing. Meas Sens. 2025;39:101879. doi:10.2139/SSRN.5081291.
9. Jiang Y, Finnegan W, Wallace F, Flanagan M, Flanagan T, Goggins J. Structural analysis of a fibre-reinforced composite blade for a 1 MW tidal turbine rotor under degradation of seawater. J Ocean Eng Mar Energy. 2023;9(3):477–94. doi:10.1007/s40722-023-00279-w.
10. Valdivia Camacho MA, Munko MJ, Cuthill F, Bradaigh CM, McCarthy ED, Lopez Dubon S. Parasitic effects of load introduction points in full-scale composite tidal turbine blade tests. Proc Annu Br Conf Non-Destr Test. 2023;2023(1):1–12. doi:10.1784/ndt2023.3a4.
11. Zavvar E, Rosa-Santos P, Taveira-Pinto F. Analysis of SCF parameters in two planar joints in offshore wind turbine support structures. J Constr Steel Res. 2025;231(5):109608. doi:10.1016/j.jcsr.2025.109608.
12. Zavvar E, Rosa-Santos P, Taveira-Pinto F, Ghafoori E. Lifetime extension of offshore support structures of wind turbines: a review. Renew Sustain Energy Rev. 2025;217(7):115788. doi:10.1016/j.rser.2025.115788.
13. Munaweera Thanthirige TR, Goggins J, Jiang Y, Flanagan M, Kennedy C, Finnegan W. Approach to develop vulnerability curves for tidal turbine blades. Ocean Eng. 2026;343:123238. doi:10.1016/j.oceaneng.2025.123238.
14. de la Torre O, Moore D, Gavigan D, Goggins J. Accelerated life testing study of a novel tidal turbine blade attachment. Int J Fatigue. 2018;114(5):226–37. doi:10.1016/j.ijfatigue.2018.05.029.
15. Finnegan W, Jiang Y, Glennon C, Flanagan M, Goggins J. Observations from structural testing of full-scale tidal turbine blades. In: Proceedings of the European Wave and Tidal Energy Conference; 2023 Sep 3–7; Bilbao, Spain. Vol. 15. doi:10.36688/ewtec-2023-277.
16. Anas SM, Tahzeeb R, Al-Dala'ien RN, Alam M, Shariq M. Widely employed constitutive material models in Abaqus FEA software suite for simulations of structures and their materials: a brief review. E3S Web Conf. 2024;497(2):02002. doi:10.1051/e3sconf/202449702002.
17. Khan MNA, Tüfekci M. Structural topology optimisation of a composite wind turbine blade under various constraints. Wind. 2025;5(4):23. doi:10.3390/wind5040023.
18. Tüfekci M, Koçak O, Özkan Y, Pir İ, Tüfekci E. Numerical evaluation of design strategies for a composite wind turbine blade: using metallic foams and optimising topology. Energy Sci Eng. 2025;13(4):1457–77. doi:10.1002/ese3.70030.
19. Duarte APC, Díaz Sáez A, Silvestre N. Comparative study between XFEM and Hashin damage criterion applied to failure of composites. Thin-Walled Struct. 2017;115(1):277–88. doi:10.1016/j.tws.2017.02.020.
20. Jiang H, Ren Y, Liu Z, Zhang S, Wang X. Evaluations of failure initiation criteria for predicting damages of composite structures under crushing loading. J Reinf Plast Compos. 2018;37(21):1279–303. doi:10.1177/0731684418783847.
21. Zhang QD, Yang F, Yang JS, Yang JS, Fan YL, Wei YY, et al. Vibration and damping properties of carbon fiber reinforced composite structures with various Poisson's ratios. Compos Struct. 2026;389(7646):120433. doi:10.1016/j.compstruct.2026.120433.
22. Krucinska I, Stypka T. Direct measurement of the axial poisson's ratio of single carbon fibres. Compos Sci Technol. 1991;41(1):1–12. doi:10.1016/0266-3538(91)90049-u.
23. Purnell P, Cain J, van Itterbeeck P, Lesko J. Service life modelling of fibre composites: a unified approach. Compos Sci Technol. 2008;68(15–16):3330–6. doi:10.1016/j.compscitech.2008.08.026.
24. Zafari B, Toby Mottram J, Purnell P, Grammatikos S, Evernden M. Hygrothermal aging of Pultruded fiber–polymer composite with predictions for design service lives. J Compos Constr. 2025;29(1):04024088. doi:10.1061/jccof2.cceng-4854.

25. Munaweera Thanthirige TR, Flanagan M, Kennedy C, Courade C, Cronin P, Georg J, et al. Advanced material strategies for tidal turbine blades: from structural validation to marine durability. In: Proceedings of the 45th International Ocean Offshore and Arctic Engineering Conference; 2026 Jun 7–12; Tokyo, Japan. New York, NY, USA: ASME.
26. Lobanova M, Aleshkevich V, Babkin A, Kepman A, Avdeev V, Morozov O, et al. Effect of post-curing temperature on the retention of mechanical strength of phthalonitrile thermosets and composites after a long-term thermal oxidative aging. Polym Compos. 2023;44(12):8330–43. doi:10.1002/pc.27699.
27. Sambayi PMK, Heyns PS. Effects of multiple post cure cycles on properties of composite carbon fibre and epoxy materials. J Compos Mater. 2023;57(15):2467–81. doi:10.1177/00219983231169333.